A three-dimensional crustal velocity model of the southwestern Alps from local earthquake tomography

[In JGR, VOL. 106, NO. B9, PAGES 19,367-19,389, SEPTEMBER 10, 2001]

Anne Paul,[1] Marco Cattaneo,[2,3] François Thouvenot,[1] Daniele Spallarossa,[2]
Nicole Béthoux,[4] and Julien Fréchet[1]

Abstract. A temporary network of 65 short-period seismological stations was installed in the southwestern Alps during the second half of 1996. It complemented the permanent monitoring networks, obtaining an average interstation distance of $\sim$ 10 km. Travel time data from 446 local earthquakes and 104 quarry blasts were inverted simultaneously for hypocenter parameters and three-dimensional velocity structure. The P wave velocity model displays strong lateral contrasts both at shallow and deeper levels. A low-velocity anomaly stands out at shallow depths beneath the Digne and Castellane nappes in the southwestern part of the investigated area. Farther east, the Monviso ophiolitic massif appears to have a much larger extension at depth than previously assumed. The largest and strongest anomaly is located under the Dora Maira massif and the westernmost Po plain. It correlates with the well-known Ivrea body, which is classically interpreted as a wedge of Adriatic upper mantle. At the best resolved depths (10 and 15 km) it appears as a rather thin (10 to 15 km), north-south elongated, high-velocity (7.4 to 7.7 km s^{-1}) anomaly with very sharp edges, extending to the south as far as 10 km north of the surface trace of the Frontal Penninic Thrust. Special care was taken with regard to the quantitative estimation of the resolution for the main anomalies using the inversion of synthetic travel time data.

1. Introduction

The Alpine belt as a whole is by far the most extensively studied orogen. However, detailed reliable information on the lithospheric structure of its southwestern termination remains scarce [*Kissling,* 1993]. The first reason for this is the complexity of the three-dimensional lithospheric structure. The few available deep seismic and gravity data suggest an asymmetric crustal root with a crust-mantle boundary separated into three or more offset subinterfaces. According to the latest model elaborated by *Waldhauser et al.* [1998] from a thorough review of available data and 3-D modeling of the Moho topography, the European Moho dips toward the east and underthrusts the south dipping Adriatic Moho, which is in turn overthrusted at its southern rim by the shallow north dipping Ligurian Moho. The precise geometry of this complex Moho topography remains unknown because of the lack of seismic data but also because available geophysical data are dominated by the effect of the shallow high-density and high-velocity Ivrea body, which masks deeper structures.

The Ivrea anomaly is the most documented geophysical feature of the western Alps [see, e.g., *Closs and Labrouste,* 1963; *Berckhemer,* 1968; *Ménard and Thouvenot,* 1984]. The Bouguer anomaly map displays a very strong positive anomaly between the Insubric Line in the north and the south of the Dora Maira Massif. It was first modeled by *Berckhemer* [1968] as a "bird-shaped," shallow (10-to-20-km depth), high-density body. Refraction and wide-angle reflection profiles recorded between 1958 and 1966 proved the existence of a high-velocity body (apparent velocity of 7.4 km s^{-1}) which was interpreted as a wedge of anomalous upper mantle [*Closs and Labrouste,* 1963; *Berckhemer,* 1968]. The Ivrea body also has a strong magnetic signature, as recognized by *Lanza* [1975] and *Froidevaux and Guillaume* [1979]. From 2-D modeling of the Bouguer anomaly combined with reinterpretations of seismic data, *Ménard and Thouvenot* [1984] proposed a new structural model based on a hypothetical flaking of the European lithosphere. In their interpretation the Ivrea body is split up into three units: the surface unit, located at very shallow depth under the Canavese and Insubric Lines, is related to the outcrops of high-grade metamorphic basic and ultrabasic rocks of the Sesia Zone and Lanzo massif (see locations in Figure 1); the main unit, at $\sim$ 10-km depth, is connected to the Frontal Penninic Thrust; and the lower unit, located at

30-km depth, is connected to the thrust of the External Crystalline Massifs onto the Subalpine basement. When this hypothesis of a lower allochthonous mantle unit was first proposed by *Ménard and Thouvenot* [1984], it relied mostly on the modeling of slight changes in the gradient of the Bouguer anomaly. This hypothesis was reinforced later by wide-angle seismic data recorded along the ECORS-CROP (Etude de la Croûte continentale et Océanique par Réflexion et réfraction Sismique - Crosta Profonda) profile (see location in Figure 1) which showed a reflector at 30-km depth below the Piemont and Briançonnais zones south of the Gran Paradiso Massif [*ECORS-CROP Deep Seismic Sounding (DSS) Group,* 1989]. It was interpreted by *ECORS-CROP DSS Group* [1989] and *Nicolas et al.* [1990] as the top of a mantle wedge sliced off from the European lithosphere by extensive flaking and by *Roure et al.* [1990] as a result of wedge-shaped indentation of Adriatic mantle into the European lithosphere. More recently, *Roure et al.* [1996] suggested that the reflector at 30-km depth could be interpreted as the top of European lower crust rather than mantle material. *Schmid and Kissling* [2000] used the ECORS-CROP seismic data, combined with the inversion of local earthquake data by *Solarino et al.* [1997], to support this idea. Their main argument is that in the tomographic results the Ivrea body appears as limited toward the west and northwest by a low-velocity anomaly located between 20- and 35-km depth, which would be incompatible with the presence of mantle material.

These contradictory interpretations demonstrate the controversy of the deep structure of the western Alps. Moreover, since most data and interpretations concentrate along the ECORS-CROP line, the need for complementary data farther south was the main motivation of this study.

Getting a precise knowledge of the crustal structure in this region is hampered by its 3-D complexity. Because of its lack of cylindricity, the southwestern termination of the Alps has never been elected as a convenient site for deep seismic reflection profiling even though a better knowledge of the crustal structure is required to constrain orogenic models and to understand the present-day strain pattern. In the framework of the Géofrance 3-D Alpes project [*Groupe de Recherche Géofrance 3D,* 1997], the main goal of which is to improve the understanding of the recent-to-present dynamics of the southwestern Alps, a passive seismological experiment was conducted by French and Italian teams in the second half of 1996. Permanent monitoring networks were densified by using portable seismic stations and more than 1000 regional earthquakes were recorded during the experiment. This paper presents the results of the local earthquake tomography conducted from this data set.

2. Data and Analysis

2.1. Data Set

Between August 1996 and January 1997, French and Italian teams installed a temporary network of 65 (of which 45 were three-component) portable seismographs in the southwestern Alps (Figure 1). It complemented the 55 (of which 6 were three-component) permanent stations of the Grenoble, Strasbourg, Nice, and Genova universities, thus decreasing the average interstation distance to $\sim$ 10 km. This experiment primarily aimed at improving our understanding of the present-day strain field of the region from precise earthquake locations and focal solutions and at imaging the 3-D structure of the upper crust by local earthquake tomography.

More than 1000 regional earthquakes with local magnitude between -0.5 and 4.2 were recorded, among which 730 could be located reliably by using an updated version of the HYPO71 program [*Lee and Lahr,* 1975] which takes station elevation into account. For the inversion of arrival times, 347 events with at least five P and three S arrivals, an azimuthal gap smaller than 180°, and an RMS smaller than 1 s were selected. It should be noted that this selected data set was verified by one person to insure the quality and the homogeneity of data that had initially been picked by different teams. At this stage, the use of the interactive picking and location software developed at the Observatoire de Grenoble (Pickev97) proved essential. The picking error is 0.01 s for P and 0.02 s for S arrivals with strongest weight, and 0.5 s for P and 1 s for S with smallest weight. The average number of picked arrivals for a single event is 33, among which 17 are P and 16 S-P. Since the maximum depth of these events is $\sim$ 20 km, we added 99 complementary earthquakes located at larger depths beneath the Po plain and recorded by the permanent network of Genova University outside the experiment period [*Cattaneo et al.,* 1999]. On average, these events have 12 P and 11 S-P picked arrivals. Finally, picks of 104 quarry blasts recorded by the Italian network were added to the data set to improve the quality of the inversion results. As a whole, the data set is made of 15,462 arrival times with nonzero weight (8194 P and 7268 S-P) for 550 events recorded at 120 stations. One hundred and three stations were located inside the study region shown in

Figure 1 (43.75°N - 45.25°N ; 6°E - 8°E), while 17 were in the near outside. A map of epicenters and the projection of all hypocenters on an east-west cross section are presented in Figure 2a. Because of the limited period of the experiment the map only partially shows the concentration of epicenters along the two seismic arcs first described by *Rothé* [1941] and imaged in detail by *Thouvenot* [1996], *Sue* [1998], and *Sue et al.* [1999]: the Briançonnais arc in the Briançonnais zone and the Piemont arc farther east. Most of the activity of the latter clusters along a remarkable N170°alignment between the southwestern termination of the Dora Maira massif and the Argentera massif. The seismicity of the external zones is more diffuse. The cross section of Figure 2a documents the increase of focal depths from west to east. While the seismicity of the external zones and the Briançonnais arc is shallower than ~ 10 km, earthquakes of the Piemont arc are located mainly between 5 and 20 km depth. Farther east, they reach depths down to 70 km under the Po plain. In their analysis of this anomalous deep seismicity, *Cattaneo et al.* [1999] even reported events with focal depths reaching 110 to 120 km. It can be expected that this heterogeneous distribution of focal depths will have a strong influence on the resolution of the inversion for layers deeper than 10 km.

2.2. Computation of the Initial 1-D Model

The solutions of an inverse problem of 3-D local earthquake tomography and their reliability strongly depend on the initial 1-D reference model, as shown by *Kissling et al.* [1994]. They claim that every 3-D inversion should start with a 1-D inversion to compute the so-called "minimum 1-D model" defined as the 1-D velocity model with station corrections and hypocenter parameters that minimizes the RMS residual of the full data set. To compute this starting model, we used a slightly different procedure from the one proposed by *Kissling et al.* [1994]. Our initial model was the minimum 1-D model computed by *Sellami et al.* [1995] from a seismicity data base covering all the western Alps. This initial velocity model includes 10 layers between -5 and 60 km with a Moho located at 38-km depth. Note that a plot of observed travel times as a function of epicentral distance shows that the data set only includes arrival times of direct waves, i.e., without any *Pn*. Velocities in layers deeper than 20 to 30 km will therefore only be constrained by arrival times from the few deep events located below the eastern part of the studied area.

We first compute an updated a priori model by conducting a series of successive 1-D inversions and relocations following the procedure described in step 2 of *Kissling et al.* [1994]. This second model is a refined version of the previous one since it includes new velocities, station corrections, and hypocenter parameters which lead to a smaller variance than the initial model. Note that no quarry blast data were included in the 1-D inversion, as suggested by *Kissling et al.* [1994]. Second, we conducted a systematic search for the minimum 1-D model. From the updated a priori model, we generated a set of 100 new V_P and V_S velocity models by introducing random changes (uniform deviates) of layer velocities as large as 1 km s^{-1} for V_P and $1/\sqrt{3}$ for V_P/V_S (see V_P models in Figure 3a). Together with station corrections and hypocenter parameters of the updated a priori model, these random velocity models were injected as initial models in the iterative inversion for an 1-D model. A plot of the velocity models resulting from the 61 inversions that converge to a variance smaller than 0.15 s^2 provides valuable knowledge of the variations of resolving power with depth (Figure 3b). Figure 3b also shows that the standard deviation on the velocities is still large for many layers, making the choice of the best model difficult. To reduce these standard deviations, we repeated the procedure. A new starting model was built by merging adjacent layers with similar velocities and suppressing too thin layers at poorly resolved depths. This new model was in turn randomly modified (maximum variations for V_P, 0.5 km s^{-1}, and for V_P/V_S, $0.5/\sqrt{3}$) to get a new set of 50 initial models which were again injected in the inversion process (Figure 3c). Since the standard deviation on the layer velocities was reduced significantly (Figure 3d), we considered the final model giving the smallest variance after this new refinement step as the minimum 1-D model. It was used down to 30-km depth as the initial V_P model in the 3-D inversion (Table 1). Because of poor resolution at large depths and also very strong lateral depth changes under the studied region, the Moho velocity jump does not appear in the results of the 1-D inversions. However, we considered a Moho depth of 50 km in the initial velocity model of Table 1 in agreement with the maximum depth measured in that region from seismic profiling. The 1-D inversions all lead to final V_P/V_S ratios between 1.65 and 1.75 for all layers except the shallowest (-5 and 0 km) and deepest (50 km) ones. Therefore we chose not to consider these rather weak depth variations of V_P/V_S, and we started the 3-D inversion from a simple homogeneous ratio (V_P/V_S=1.71) estimated from a Wadati diagram of the travel times T_S versus T_P. The hypocenter loca-

Table 1. Initial 1-D Velocity Model for the 3-D Inversion

Depth, km	V_P, km s^{-1}
-5	5.00
0	5.70
5	6.00
10	6.20
15	6.45
20	6.49
30	6.94
50	8.00

tions computed in the minimum 1-D model and plotted in Figure 2a were also used as initial reference for the 3-D inversion.

The main advantage of this procedure is that it guarantees the independence of the final 1-D model with respect to the updated a priori model by probing a large part of the solution space. Note that we conducted this set of 1-D inversions by using both programs VELEST [*Kissling et al.,* 1984], which assumes constant velocities in layers, and SIMULPS [*Thurber,* 1983, 1993; *Eberhart-Phillips,* 1993], which interpolates velocities between layers of nodes. The two programs gave similar results. With respect to a reference station in the Briançonnais zone, we found negative station delays east of longitude 7°E in the region of the Ivrea body with a maximum delay of -0.7 s. Strong positive corrections as large as 1 s were found in the southwestern corner of the studied region.

To evaluate the uncertainty on absolute event locations in the minimum 1-D model, we used randomly shifted hypocenters as initial locations for an inversion for hypocenter location and measured the average shifts in final locations. As suggested, for example, by *Haslinger et al.* [1999], a random shift between 6 and 8 km was applied in each direction to every hypocenter. The differences between relocated randomly shifted hypocenters and initial locations of the minimum 1-D model are, on average, 1 km in the vertical and 150 m in the horizontal directions for the 347 events of the temporary experiment data set, and 2.5 km in the vertical and 300 m in the horizontal directions for the 99 complementary events recorded by the permanent Italian stations only. Another possible way to assess absolute locations is to shift blasts, but since they are concentrated in the Italian side of the model and recorded by Italian permanent stations only, this method cannot provide a reliable uncertainty estimate for the whole area.

2.3. The 3-D Inversion Approach

Arrival times were inverted simultaneously for velocity (V_P and V_P/V_S) and hypocenter parameters using the now classical FORTRAN program SIMULPS (v. 12) by *Thurber* [1983, 1993] and *Eberhart-Phillips* [1993]. Starting from a 1-D velocity model and the corresponding preliminary locations of hypocenters, SIMULPS uses an iterative damped least squares inversion technique to compute V_P and V_P/V_S at nodes of a 3-D grid and new event locations that minimize the residuals between observed and computed travel times. Travel times in the 3-D model are computed using the approximate ray-tracing technique of *Um and Thurber* [1987]. Velocities are interpolated linearly between grid points.

Critical parameters of the 3-D inversion are the grid spacing, the damping values, the number of iterations, and the initial 1-D velocity model. Our reference model was the minimum 1-D model computed with the VELEST program and presented in section 2.2. To assess the influence of the initial model on the inversion results, we made tests using the 1-D model of *Sellami et al.* [1995] and the minimum 1-D model computed with the SIMULPS program as starting models. All the inversions gave similar results as far as the distribution of the main velocity anomalies is concerned. However, these tests showed, as expected, that the absolute velocities must be considered with caution since they differ when different initial velocity models are considered.

The grid nodes used in the inversion are shown in Figure 2b. The grid area is 160 km wide in the north-south and east-west directions. In the vertical direction we tested a number of different grids with spacings comprised between 2 and 5 km for the shallowest layers. We finally chose to present the results obtained with the coarsest grid with node layers at -5, 0, 5, 10, 15, 20, 30, and 50 km depth. This grid divides the model in more regular blocks than the 2-km spacing and is therefore expected to be less prone to vertical leakage, although our tests did not show significant differences. Only the outer nodes and those of the 50-km-depth layer were held fixed in the inversions. Since the study area is located at the southern termination of the Alpine arc where many structural directions interfere, the choice of the grid orientation was not obvious. We made the most simple choice of a north-south/east-west grid. We tested another grid aligned parallel to the Pelvoux-Argentera axis (i.e., N135°), which led to very similar tomographic images. The density of stations and earthquakes was high enough to allow the use of a lateral grid spacing of 10 km. In the southern half of the Dora Maira Massif where the strong anomaly related to the Ivrea body is expected and where much of the seismicity is concentrated, we reduced the lateral spacing to 5 km (Figure 2b).

Following the suggestion of *Eberhart-Phillips* [1993], we tested two inversion procedures, the direct approach where data are inverted directly for the finely gridded 3-D model and the gradational approach where a progressive series of inversions is done on more and more detailed grids. In the gradational approach we inverted first for a coarse model with a 40-km grid (Figure 2b); then velocities of the 40-km grid were interpolated linearly with a 20-km grid. This new starting model and relocated hypocenters were in turn used to invert for a 20-km grid model and so on to the finest gridded model with 10- and 5-km spacing. The gradational approach is more natural than the direct one since it first captures the long-wavelength anomalies before adding progressively smaller details. For this reason, it is expected to give more accurate results and a larger variance reduction [*Hauksson and Haase,* 1997]. However, it was not the case in this study where both the direct and gradational inversions resulted in similar variance reductions (49 and 48%, respectively, see Table 2). A possible explanation is that we let the model evolve by keeping the damping parameters fixed for all the iterations while others [e.g., *Hauksson and Haase*, 1997], use a variable damping that increases with increasing model length, which stops the model changes very early. Another explanation may be the very uneven grid spacing with blocks 40 or 20 km in the horizontal directions and only 5 km in the vertical direction which can lead to very poor resolution.

The tomographic images differ only in detail and the result of the gradational inversion appears as a filtered version of the model obtained from the direct inversion with the smallest wavelengths removed.

To find the best damping parameters, we ran a series of single-iteration inversions with a large number of couples of damping parameters on V_P and V_P/V_S between 1 and 1000. By plotting data misfit versus model variance, we can determine the damping value which is the optimal compromise between a small data misfit and a large model variance. Our tests showed that the two damping parameters could be chosen independently as the inversion for a V_P model did not depend on the damping on V_P and V_P/V_S and vice versa. All our tests showed that this was not the case and that the two damping parameters could be chosen independently. For the direct inversion for the fine-gridded model, we also checked the linear behavior of the inversion by running tests with different damping values and different maximum number of iterations. We verified that with a larger number of iterations and a stronger damping (200), the inversion gave roughly the same model as the one resulting from less iterations and a weaker damping (100). To avoid strong and unrealistic anomalies in the V_P/V_S model, we used a larger damping for V_P/V_S (400) than for V_P (100). This also accounts for the different qualities of picks on P and S arrivals. As mentioned earlier, these damping values were held constant for all iterations. We decided to stop iterating when the reduction of data misfit was becoming negligible (i.e., smaller than 3%) that is after 6 iterations for the direct inversion. For the gradational inversion we conducted the damping tests at each inversion step. The selected values of the damping parameters are given in Table 2. Three iterations of inversion were done at each step. Figure 4 shows data misfit as a function of model length for both inversion approaches. Note that they both end with similar data and model variances for the P data set.

Table 2. Data and Model Variances for the Initial 1-D Model and the Two 3-D Models DIR and GRAD.

			Global	P		S-P	
	Damping		Data Variance	Data Variance	Model Variance	Data Variance	Model Variance
Model	P	S-P	s^2	s^2	$(km\ s^{-1})^2$	s^2	$(km\ s^{-1})^2$
Initial	-	-	0.10773	0.05228	0	0.11230	0
DIR	100	400	0.05514	0.01948	0.04448	0.06997	0.00027
GRAD	3000/500/100	3000/1000/400	0.05636	0.02007	0.05168	0.07111	0.00038

Initial data variances were measured after relocation of hypocenters by SIMULPS in the minimum 1-D model (iteration 0). Model DIR results from six iterations of the direct inversion for the finely gridded velocity model. Model GRAD results from the gradational inversion (three inversions of three iterations each using progressively finer grids).

As usually done in local earthquake tomography, data recorded at large epicentral distances were weighted using a linear taper decreasing from 1 at 100 km to 0 at 150 km. This weighting aims at attenuating the effects of large residuals related to the longest ray paths, not only due to mistakes in phase identification, but also to mismodeling of the true ray paths. However, we checked on synthetic models that the distance weighting has a weak influence on this tomography because most data were recorded at epicentral distances shorter than 70 km. To remove high residuals corresponding to erroneous arrival times, we also applied a residual filter with a linear taper from 1 at 1 s, to 0.02 at 1.75 s, with a cutoff at 2.75 s.

2.4. Estimation of the Quality of the Results

Evaluating the quality of the obtained 3-D velocity models requires a close examination of many parameters including the resolution matrix, the distribution and the direction of the rays. Following *Toomey and Foulger* [1989] and *Michelini and Mac Evilly* [1991], we computed the spread function of the resolution matrix to estimate how well velocity parameters were resolved. At a given node this spread function is computed as

$$S_i = \log\left(\mid R_i \mid^{-1} \sum_{j=1}^{N} \left(\frac{R_{ji}}{\mid R_i \mid} \right)^2 D_{ij} \right)$$

from all the terms R_{ji} of the corresponding column of the resolution matrix. A weighting by the distance between nodes D_{ij} is applied before summing the contributions of adjacent nodes. $\mid R_i \mid$ is the L2 norm of the terms of the line of the resolution matrix. The spread function is a better estimator of the resolving power than the diagonal element of the resolution matrix because it takes all the terms of the resolution matrix in account. A well-defined parameter has a small resolving width and thus a small spread function. Note that following the suggestion of the authors of SIMULPS [*Evans et al.,* 1994], we chose to calculate the resolution matrix on the first iteration because it produces the largest variance reduction. Another estimator of the suitability of data for a reliable tomography is the derivative weight sum which describes the amount of data actually constraining the velocity at a given node [*Evans et al.,* 1994]. It is computed from the hit count weighted by the inverse of the ray node distance and the ray length in the vicinity of the node. Figure 5 compares the values of the spread function with the diagonal of the resolution matrix (DRM) and the derivative weight sum (DWS) for all the nodes of the direct inversion for the finely gridded velocity model. Note that nodes with similar DWS or DRM have different spread function values, showing that neither of these two parameters can be used alone to evaluate the inversion quality. These plots were used to define a threshold of spread function above which the results of the inversion would not be shown on the velocity maps because they correspond to unresolved nodes. We chose empirically to set the threshold at 6 for V_P and 6.5 for V_P/V_S because larger values of the spread function definitely correspond to too small values of DWS and DRM (Figure 5).

As emphasized above, the spread function is used here to estimate the area of confidence in the 3-D velocity model. We consider that outside this area the resolution parameters are too low to allow the presentation of any result. However, this does not mean that we automatically consider the results inside the area of confidence as reliable since the spread function only gives a crude qualitative estimate of the actual resolution. The only way to really quantify resolution is by synthetic data tests that mimic structures derived from the tomography and use the actual distributions and combinations of earthquakes and stations. A comparison of the initial and final models gives more reliable insight on the resolving power of the tomography than any function calculated from the resolution or correlation matrices. The results of these synthetic data tests will be discussed together with the tomography results in section 4.

3. Results

3.1. Preferred V_P 3-D Model

We choose to show only the results of the direct inversion (model DIR) because tests on synthetic data sets show that the output velocity model is much closer to the input model when it is computed with the direct inversion than with the gradational one, as the latter leads to too smooth anomalies. Note, however, that most of the subsequent comments on velocity anomalies would have been identical if based on the results of model GRAD.

Plate 1 shows maps of P wave velocity at the different node depths between 0 and 30 km. These maps were computed from a linear interpolation of velocity values between nodes using the same routine as the one used in the SIMULPS program for ray tracing. As explained in section 2, the velocity color maps are only shown inside the 6 contour of the spread function; outside of it, the model is not resolved. We included the 5 and 4 contours (thick and thin white lines) to show how the spread function evolves around the chosen resolution limit of 6. Hypocenters located within the depth range of the layer are drawn as white circles. The size and shape of the area of confidence are naturally correlated with the depth distribution of hypocenters. This area covers the edge of the external zones, the Penninic zone (Briançonnais and Piemont zones), and most of the Dora Maira internal crystalline massif at shallow depths, before progressively reducing in size and shifting eastward with depth as the deepest hypocenters are concentrated beneath the eastern part of the study area (Figure 2a).

This section includes a summary of the main anomalies from the map views of Plate 1 and cross sections through the model. Discussions on the reliability of the anomalies and their geological interpretation will be presented in section 4.

A thick and strong low-velocity anomaly is visible in the 0-, 5- and 10-km map views beneath the Digne and Castellane nappes at the southwestern edge of the area of confidence. A few other low-velocity anomalies are imaged at 0-km depth mostly in the Penninic zone, with the largest located north east of Argentera. A strip of discontinuous high-velocity anomalies is found at 0-km depth under the Piemont zone along the western border of Dora Maira. On the 5-km-depth slice the strongest and largest high-velocity anomaly is a north-south elongated body extending from the southern half of the Monviso ophiolite surface outcrop to the Frontal Penninic Thrust (FPT) surface exposure. P wave velocities reach between 6.2 and 6.7 km s^{-1} in this body.

The strongest anomaly of the 10-km slice is a rather thin and north-south elongated high-velocity anomaly located under Dora Maira and under the Penninic zone between the Dora Maira and Argentera massifs. This high-velocity body extends at depth down to the deepest layer of the model at 30 km. It is most clearly visible at 15 km with maximum velocities between 7.4 and 7.65 km s^{-1}. The anomaly attenuates at 20 km, but the contours of the spread function suggest that the velocity model is more poorly resolved at 20 km than at 15- or 30-km depth.

To improve the visualization of the results, we plotted four cross sections through the 3-D model in Plate 2. Cross sections A, B, and C are perpendicular to the axis of the deep high-velocity anomaly while cross section D is perpendicular to the Frontal Penninic Thrust (FPT) between the Dora Maira and Argentera massifs. Sections A, B, and D cross all the main structural domains of the southwestern Alps, from the external zones to the internal crystalline massif of Dora Maira across the Penninic zone. Note that the FPT is the main structural boundary imaged farther north by the ECORS-CROP deep seismic reflection profiling (*Nicolas et al.* [1990], see Figure 1 for the location of the ECORS-CROP profile). It is considered as a crustal-scale thrust of the internal zones onto the external zones. In between the Pelvoux and Argentera crystalline massifs and under the western termination of lines A, B, and C, the external zone is overthrusted by a thin nappe of internal origin, the "Flysch à Helminthoïdes" nappe (Figure 1). As a consequence, the actual FPT is located at the front of the nappe in this region. However, this nappe is very thin, and we chose to follow the suggestion of *Sue and Tricart* [1999] to consider in this region the Frontal Briançonnais Thrust (FBT) as the surface expression of the main crustal-scale thrust. Its location and the limits of the surface exposures of the crystalline massifs are shown as black triangles on top of each of the sections of Plate 2.

Cross sections A and B show relatively low velocities, around 5.5 km s^{-1}, down to 10-km depth under both the easternmost external zone and the Penninic zone. Farther east, the Penninic zone is separated from the Dora Maira massif by a high-velocity anomaly which rises up to the surface. This anomaly was mentioned previously in the discussion of the map views as the high-velocity structure for which the surface trace coincides with the Monviso ophiolites. The Dora Maira massif is underlain by relatively low velocities contrasting sharply with the deeper and strong high-velocity anomaly which dominates the 15-km-depth map view.

Cross section D is perpendicular to the FPT and roughly parallel to the average shortening direction of the foreland Digne and Castellane nappes. The crustal structure of this part of the southwestern Alps is quite poorly known, and it can hardly be extrapolated from controlled-source seismology data recorded along the ECORS-CROP line situated some 200 km farther north in a region where the shortening axis is directed toward the northwest. Once again, cross section D shows low velocities under the external (including Argentera) and Penninic zones as well as under the Dora Maira massif. The Penninic zone is bounded to the northeast by a rise of high velocities close to the surface. A striking feature is the large thickness of the low-velocity layer under the Argentera massif where velocities as low as 5.5 km s^{-1} are found at depths larger than 10 km, reaching nearly 15 km under the northern edge of the crystalline massif. Note, however, that Plate 1 shows that this thick low-velocity layer is found only under the western half of the Argentera crystalline massif surface exposure, whereas its eastern half is characterized by velocities above 6 to 6.5 km s^{-1} from 5-km depth and below.

In cross sections C and D, the shallow low-velocity layer of the Penninic zone is thinner than in cross sections A and B because of the presence of the southern termination of the deep high-velocity body below it. This is a major difference with respect to the northern regions where the 15-km depth high-velocity anomaly does not extend westward beyond the boundary between the Dora Maira massif and the Penninic zone. South of Dora Maira, the Ivrea body spreads under most of the Penninic zone as far as 10 km north of the surface exposure of the FPT.

3.2. V_P/V_S Model

Travel time differences between S and P waves were inverted for the V_P/V_S ratio. As explained earlier, the initial model was homogeneous with V_P/V_S equal to 1.71 at all nodes. This value was estimated from a Wadati diagram of the travel times T_S versus T_P. Measurements of V_P/V_S lead to estimations of the Poisson's ratio giving information on the fluid content in porous rocks and on the petrologic nature of the crust at high pressures where porosity is eliminated [*Christensen,* 1996].

Map view slices of the V_P/V_S 3-D model for the three shallowest layers are shown in Plate 3. Results at larger depths are not shown because they are almost completely devoid of anomalies. This rapid attenuation of the V_P/V_S heterogeneity with depth is clearly visible from the map views of the three shallowest layers presented in Plate 3. The question is to determine whether this attenuation is real or a consequence of a degradation of resolution with depth. Comparing the map views of the V_P model at 0, 5, and 10 km (Plate 1) with those of the V_P/V_S model (Plate 3) shows that according to the criteria based on the threshold in spread function, the fairly resolved areas are systematically smaller for V_P/V_S than for V_P. However, since the choice of the threshold is empirical and, as explained before, the spread function gives only a qualitative estimate of the resolution, we checked the resolution with synthetic tests. Synthetic data sets were computed by SIMULPS from models with V_P/V_S anomalies located at all depths under the Dora Maira massif, which is the region crossed by the largest number of rays. These tests proved that if the deep high-V_P body located from 10-km depth and below under Dora Maira was also characterized by a V_P/V_S anomaly equal to or larger than ±5%, the inversion would be able to resolve it. The resolution of the V_P/V_S model is comparable to that of the V_P model probably because our data set includes nearly the same numer of P and S-P time picks. We therefore consider that the rapid attenuation of V_P/V_S anomalies with depth is reliable. The distribution of V_P/V_S anomalies is very different from the distribution of V_P anomalies. The 0-km-depth slice shows two regions of anomalously high V_P/V_S in the Penninic and external zones between 6.5 and 6.8°E longitude and between the Dora Maira and Argentera massifs. The main low V_P/V_S anomaly is found beneath the western half of the Argentera massif.

4. Discussion: Quality of the Results and Structural Implications

As emphasized in section 2, the quality of the 3-D velocity model can only be assessed reliably from synthetic data tests. Therefore a series of synthetic 3-D V_P and V_P/V_S models were built which included the main anomalies described in section 3. The synthetic input model and the result of the inversion of the synthetic data set are presented in Plate 4 for V_P and Plate 5 for V_P/V_S. In Plates 4 and 5, the results of the inversion of the synthetic travel times are compared to those of the inversion of the observed travel times. This comparison is facilitated by displaying the V_P and V_P/V_S as variations relative to the initial 1-D model, rather than as absolute values.

The 0-km depth node plane of the input V_P model (Plate 4a) includes the two strongest and largest low V_P anomalies in the southwest corner of the model and northeast of the Argentera massif. The southwestern anomaly continues down to 10-km depth with a reduction in size. A few small-scale high-V_P anomalies are added in the 5-km-depth node layer to mimic the results depicted in Plate 1. The strongest one, located along the western border of the Dora Maira massif, has a velocity of 7.0 km s^{-1}. From 10-km depth and deeper, a 10 to 30 km thick north-south elongated high-V_P body with a slight eastward plunge is introduced in the synthetic model to mimic the strong, deep high-velocity anomaly described above.

Synthetic travel times were computed first in the synthetic input 3-D velocity model with hypocenter locations held fixed and using the same event and station distribution as in the actual data. A uniformly distributed random noise was added to the synthetic travel times in the range -0.2 s to +0.2 s for P arrivals and -0.4 to +0.4 s for S. They were inverted using the same procedure and parameters as for the observed data. Note that numerous tests were made with different geometries and velocities for all anomalies, particularly the deep high-velocity body. The model presented here is the one which gives the best fit between the output of the inversion of synthetic travel times (shown in Plate 4b) and the velocity structure calculated from the inversion of real data (shown in Plate 4c).

4.1. External Nappes

As already emphasized, the velocity distribution at shallow depths (Plate 1) shows a thick low-velocity anomaly under the Digne and Castellane external nappes. The synthetic tests of Plate 4 show that the geometry of the corresponding anomalous body is rather well resolved at its northeastern border in the 0- and 5-km-depth slices. At 10 km a smaller number of rays probably induces a worse fit to the input model. However, the anomaly is still visible at this depth in the inversion of real data (Plate 4c). This is probably a reliable indication that the total thickness of the low-V_P body reaches 10 km. This very unexpected anomaly is the second biggest volume of anomalous P velocity in the area. Moreover, the amplitude of the velocity reduction is probably underestimated, as shown by the quite large positive average residuals, which are still computed for stations located in that region after 3-D inversion. This underestimation is also a general feature of the inversion as shown from a comparison between Plates 4a and 4b. This anomaly coincides with the negative gravity anomaly discussed by *Masson et al.* [1999] from their new Bouguer anomaly map of the western Alps compiled from old data and new measurements. According to the cross sections built by *Ritz* [1991] the thickness of the nappe pile, 5 km, is compatible with both the gravity and the velocity anomaly. However, such anomalies could also be related to Permo-Carboniferous basins hidden under the nappe pile [*Ménard and Molnar,* 1988].

4.2. Argentera External Crystalline Massif

Argentera is the only external crystalline massif for which the deep structure is imaged in this study. It displays unexpected characteristics, with an anomalously large thickness of low velocities down to more than 10 km in its western half and a low V_P/V_S ratio. The map view slices at 5, 10, and 15 km seem to reveal a lateral change in the deep structure of the massif with lower than average velocities under its western half contrasting with the higher velocities of the eastern half. However, the synthetic tests of Plate 4 show similar low P velocities below the western part of the massif at 10 and 15 km depth, whereas no anomaly was introduced in the input model at this location. Thus we cannot take for granted that this lateral change in velocity structure is not an artefact of the inversion. As shown by Plate 5a, we also tested the low V_P/V_S anomaly under the western part of Argentera in both the 0- and 5-km depth node planes. Plate 5b shows that the resolution can be considered as good and that the anomaly is probably real. The low V_P/V_S values of 1.60 to 1.70 found under the Argentera massif down to 5-km depth correspond to a Poisson's ratio between 0.18 and 0.24. This indicates that rocks in the Argentera massif are nearly devoid of pore fluids. It could also be an indication of a high weight percent of SiO_2 around 80% according to the measurements made on rock samples by *Christensen* [1996].

4.3. Penninic Zone and Monviso Ophiolites

In the 0-km-depth map view the Penninic zone is characterized by P velocities similar or slightly lower than in the 1-D inital model (5.7 km s^{-1}) in its western and southern parts and by a discontinuous strip of high-velocity spots along its border with the Dora Maira massif (Plate 1). The high-velocity body located under the surface outcrop of the Monviso ophiolite and south of it is the main anomaly visible in the area at 5-km depth. At 0 km, we only tested the resolution in the region of the low-V_P anomaly located northeast of Argentera. Plate 4b shows that this anomaly is reliable. At 5-km depth, synthetic tests focused on the high-velocity anomalies which show some spatial correlation with the main ophiolite surface outcrops like the Chenaillet ophiolites east of Briançon and the southern tip of the Monviso ophiolites at the eastern boundary of the Penninic zone. Plate 4b shows that the resolution is sufficient to trust the presence of the Monviso anomaly. It is not as clear for the other anomalies which had lower velocities in the input model of Plate 4a. However, it is worth noting that the anomalies at 5 km leak onto the 0-km-depth slice. Their presence at the surface in the inversion of the observed data set could consequently be an artefact of the inversion.

As a whole, the Penninic zone appears as a high V_P/V_S region at 0-km depth as well as the southern part of the "Flysch à Helminthoïdes" nappe in the external zone. The synthetic V_P/V_S tests of Plate 5 show that the resolution is good for the three high V_P/V_S anomalies found in these two regions, except for the amplitudes of anomalies which are attenuated. Since high values of V_P/V_S are often an indicator of the presence of water-saturated cracks or high pore fluid pressure, the presence of such anomalies in the shallow sediment cover of the Penninic and external zones is not surprising.

The Monviso high-V_P anomaly is the most important both in amplitude and spatial extent at shallow depths. As shown from cross sections A, B, and C of Plate 2, it forms a more or less continuous body from the surface down to 5 km with velocities as high as 6.3 to 6.7 km s^{-1} at this depth. These values are reliable as documented by the synthetic test of Plate 4. An important point is that the anomaly is shifted southward with respect to the Monviso ophiolite outcrop. Its southern limit coincides with the FPT surface trace, 20 km south of the ophiolite surface exposure. In the cross sections of Plate 2, the shallow part of the body responsible for this "Monviso anomaly" is very clear, due to its position between two low-velocity regions under the Penninic zone and the Dora Maira massif. Its maximum vertical extension is less clear but according to cross sections A, B, and C of Plate 2, it could extend at least down to 10 km, which is the largest depth where the velocity model is reliable in this place. The four depth cross sections suggest that this "Monviso anomaly" edges the stronger high-velocity anomaly of the Ivrea body. We interpret it as a thick slice of eclogitized ophiolites in agreement with structural and petrological observations [*Schwartz et al.,* 2000]. The tomography suggests a much greater extension at depth of the Monviso ophiolite body than expected from models based on magnetic data. *Lanza* [1975] showed that the total intensity of the magnetic field is affected by a strong anomaly of 4000 nT with an approximate width of 15 km along a profile that crosscuts the southern part of the Monviso ophiolite outcrop (Plate 6). He interpreted this anomaly by a 2-to-3-km-thick slab dipping to the west at 30° down to a maximum depth of 7 km. Since his profile roughly coincides with cross section A of Plate 2, we drew Lanza's high-susceptibility body on the tomography result in Plate 6 for comparison. The magnetic body appears to extend farther west than the high-velocity anomaly, which is more vertical. Also, the velocity anomaly is thicker and extends to greater depths. A possible explanation for these differences would be that rocks with strong magnetic susceptibility are located only in the shallow part of the Monviso ophiolite body. Note that *Lanza* [1975] also discovered a strong but much thinner (3 km) total intensity anomaly along another cross section cutting the northern part of the ophiolite outcrop. He interpreted it by a much smaller magnetic body. This observation agrees with our tomography results which show the high-velocity body only under the southern part of the outcrop and farther south.

4.4. Ivrea Body

The position of the deep strong high-velocity anomaly indicates that it is obviously related to the Ivrea geophysical body. At depths equal to or greater than 10 km, it appears as a north-south elongated high-velocity anomaly located beneath the Dora Maira massif and shifting progressively eastward with depth (Plate 1). The strongest anomalies are found at 15- and 30-km depths. They are weaker at 10 and 20 km.

Since a precise mapping of the Ivrea body in 3-D was the main objective of this study, special care was taken to check the reliability of the geometry and amplitude of the related velocity anomaly. Most of our synthetic tests focussed on this anomaly. In the final input model of Plate 4a, the Ivrea body is modeled as a 10 to 30 km thick north-south elongated prism with a roof at 10 km and a slight eastward plunge. Its velocity is 7.4 km s^{-1} at 10 km as measured from refraction data [*Closs and Labrouste,* 1963; *Berckhemer,* 1968]. At 15, 20, and 30 km we had to increase the input velocity to 7.8 km s^{-1} to keep the anomalies of the output model (Plate 4b) as close as possible to the ones obtained by inversion of observed data (Plate 4c). The geometry of this prism approximately mimics the high-velocity anomaly of Plate 4c. The first observation that can be made from the result of the inversion of the synthetic data set (Plate 4b) is the vertical smearing of the high-velocity anomaly at 5 km and to a much lesser extent at 0 km. Note that on both depth slices the leakage induces a series of artificial anomalies which are very similar both in amplitude and position to the ones computed by inversion of observed data (shown in Plate 4c), particularly north of 45°N. We can conclude from this observation that the depth to the roof of the actual Ivrea is probably very close to 10 km in this area. Note that the same depth was measured by *Closs and Labrouste* [1963] using refraction profiling between Briançon and Torino in the northern part of our study region.

The comparison of Plates 4a, 4b and 4c also gives insights on the quality of the image at 10 and 15 km which are the best resolved depth slices as far as the Ivrea body is considered. First, it confirms what can also deduced from the examination of the spread function contours: the resolution varies significantly along the strike of the body, inducing artificial variations of the anomaly strength and shape. For example, Plate 4c documents an attenuation of the anomaly at 10-km depth and 44.7°N which can also be seen in Plate 4c, whereas the synthetic input model is continuous in this place. The disappearance of the anomaly north of 45°N on both the 10- and 15-km-depth slices which also appears both in Plates 4b and 4c is clearly an artefact of the heterogeneous ray coverage. Second, the comparison of Plates 4a and 4b shows that the boundaries of the anomaly are well resolved in its southern part, both for the lateral and the southern limits. This is particularly true at 10 km where the inversion is able to retrieve the thinning of the anomaly at its southern tip. The definition of the western limit is very good south of 45°N, which suggests that the sharp western boundary documented by Plate 4c is reliable. We can also trust the observation that the Ivrea seismic body extends to the south as far as 10 km north of the surface trace of the FPT. This result was confirmed by other synthetic tests where we checked that a southward or northward 10-km shift of the southern extremity of the anomaly is retrieved by the inversion. Other tests also confirmed the ability of the inversion to image a very thin (5 km) body. Finally, one can note that the inversion is unable to retrieve the amplitude of the anomaly and its very sharp edges. Actually, only a few nodes of the 10-km plane reach a velocity larger than 7.2 km s^{-1} after inversion, although the input velocity was 7.4 km s^{-1}. The same observation can be made for the 15-km node plane, and the misfit is even larger at 20 km. As already mentioned for other anomalies of the model, this misfit shows that the velocities resulting from the inversion are underestimated. However, the good similarity between the output of the synthetic model (Plate 4b) and the result of the inversion of the real data (Plate 4c) shows that the actual geometry and amplitude of the Ivrea P velocity anomaly could be very close to the input model of Plate 4a.

The depth slices at 15, 20, and 30 km in Plates 4b and 4c display anomalies of similar magnitudes, with an attenuation of the anomaly strength at 20 km with respect to 15 and 30 km. Consequently, the continuous homogeneous prism of Plate 4a leads after inversion to a discontinuous velocity anomaly with an artificial weakening at 20 km which could be due to the change in spacing between node layers at 30 km. This shows that the apparent attenuation of the anomaly strength at 20 km, which could be interpreted as a division of the Ivrea body in two units, is also an artefact of the ray coverage. This was also somewhat apparent from the spread function contours in Plate 1. We also tested that the weakening of the anomaly at 20 km is not simply the result of vertical smearing from a deeper high-velocity body. A synthetic model was constructed in that aim, with a high-velocity anomaly restricted to the 15- and 30-km-depth layers and no anomaly at 20 km. This test proved that the vertical leakage of a vertically discontinuous high-velocity body cannot explain the anomalies observed at 20 km. At 30 km the comparison of Plates 4a and 4b shows that the resolution of the eastern limit is reasonable. Since there is no such sharp boundary in the "observations" (Plate 4c), we conclude that the high-velocity body extends farther east than what was considered in Plate 4a. Note that the strengthening of the V_P anomaly at 30 km in the inversion of observed data (Plates 1 and 4c) can result from the limitation of the inversion to this depth, inducing an artificial mapping of deeper anomalies onto the bottom model border. However, we checked by enabling changes in the velocities of the 50-km-depth node layer that this effect remains weak.

A striking point that can be emphasized from Plates 1 and 2 is the concentration of hypocenters of the Piemont seismic arc at the western edge of the high-velocity Ivrea body between 10- and 20-km depth. Struck by the coincidence between the seismic arc and the western flank of the Bouguer gravity anomaly, *Thouvenot* [1996] had first described this feature. Deeper seismicity located between 15 and 30 km under the eastern edge of Dora Maira and the westermost Po plain appears more to be distributed inside the anomaly than concentrated along one of its edges. Note that the seismicity of the Piemont arc appears more diffuse and less clearly related to the Ivrea anomaly in cross section D because the cross section is not perpendicular to the trend of the seismic arc (the angle between them is $\sim 45°$). As already mentioned, no V_P/V_S lateral variation is related to the Ivrea P velocity anomaly.

Figure 6 shows a comparison between the so-called Ivrea gravity anomaly and the P wave velocity map at 15 km. The spatial coincidence between the two anomalies is acceptable, although the gravity high is shifted eastward with respect to the high-velocity spot. This shift could be explained by the eastward plunge of the high-velocity prism with increasing depth documented, for example, in Plate 2, or by strong lateral changes in Moho depth which also affect the Bouguer anomaly. The continuity of the dense body in the north-south direction expected from the continuity of the Bouguer anomaly does not stand out in the velocity maps. As mentioned earlier, this lack of continuity toward the north is an artefact of the heterogeneous distribution of ray paths.

5. Conclusions

The Ivrea geophysical body is the most puzzling anomaly in the crustal structure of the western Alps and is even one of the most remarkable anomalous features related to the deep structure of any mountain range. Getting a better resolution 3-D image of the related high P velocity anomaly was the main objective of this study. A dense network of portable seismographs was deployed in that aim during the second half of 1996, which, in complement to the permanent monitoring stations, reduced the interstation distance to $\sim$ 10 km. Although it remains moderate, the level of seismicity is higher in the southwestern termination of the Alps than in most other places in this mountain range, which was another reason why this study zone had been selected for a local earthquake tomography experiment. Thanks to the density of the network and to the addition of a number of deep earthquakes located under the Po plain and recorded by the permanent network of Genova university outside the experiment period, we succeeded to calculate images of the crust of the southwestern Alps with unprecedented high resolution. As documented by synthetic data testing, the horizontal resolution is 5 km. Because of the preferred orientation of the ray paths in the vertical direction (small-magnitude earthquakes are often only recorded by stations located above their foci), the resolution was $\sim$ 10 km in the vertical direction.

The present study also covers an area of the Penninic and external zones of the southwestern Alps which had never been probed by active or passive seismological imaging techniques. At shallow depths the tomography reveals a rather thick low velocity anomaly in the region of the Digne and Castellane nappes. Although the anomaly is clearly visible, its amplitude is certainly underestimated due to the poor ray coverage in that zone as shown by the average station residuals which remain strongly positive after inversion. This velocity anomaly coincides with a gravity low in the new Bouguer anomaly map of the southern Alps [*Masson et al.,* 1999] and is interpreted as the image of the thick sedimentary sequence of the nappe pile or as an indicator of a hidden basin buried beneath the nappes. A second outstanding result is the high-velocity anomaly detected beneath the Monviso ophiolite surface exposure. The size of the anomaly indicates that the ophiolitic body has a greater extension at depth than what was expected considering the limited size of the surface outcrop and the modeling of the magnetic anomaly by *Lanza* [1975]. The high-velocity body (very clear in the 5-km-depth slice of the 3-D model) is also shifted southward with respect to the surface exposure, in agreement with the northward attenuation of the magnetic anomaly. This result is an important element for the construction of new crustal-scale interpretative structural cross sections of the range and a better understanding of the Alpine orogeny [*Schwartz et al.,* 1999; *Schwartz,* 2000].

As pointed out above, this local earthquake tomography provides the first direct image of the southern termination of the Ivrea body. It is characterized by a strong velocity anomaly with very sharp edges. The top part of the anomaly at 10 km is rather thin (east-west extension of 10 to 15 km) and stops abruptly 10 km north of the surface trace of the FPT between the Dora Maira and Argentera crystalline massifs. A striking point is the concentration of hypocenters of the Piemont arc on the western edge of the velocity anomaly. We can therefore suggest a clear relationship between the crustal structure and the present-day stress field within the belt. The deeper events beneath the eastern flank of the Dora Maira massif and the westernmost Po plain, which were referred to as the Padane arc by *Thouvenot* [1996], appear, on the contrary, to be located inside the high-velocity anomaly.

Using the inversion of synthetic sets of travel times, we have shown that the high-velocity body is more probably continuous with depth than separated in two distinct units. Unfortunately, the lack of resolution north of 45°N at 10- and 15-km depth makes it impossible to image the along-strike variations in strength or shape of the high-velocity anomaly. Farther north (at 45.5°N), a new crustal-scale cross section of the western Alps, recently proposed by *Schmid and Kissling* [2000] from the ECORS-CROP deep seismic profile in combination with the local earthquake tomography (LET) by *Solarino et al.* [1997], did not show any indication of a separation of the body in two units. It is, however, questionable whether the resolution of their LET is sufficient to image such a separation.

Because of the lack of ray paths crossing the western part of the model at depths larger than 15 km, this inversion provides no constraint on a possible extension of the deeper part of the body westward beneath the Briançonnais zone as hypothesised by *Ménard and Thouvenot* [1984]. Note that *Schmid and Kissling* [2000] reject this hypothesis and propose that the reflector imaged by fan profiles during the ECORS-CROP seismic experiments [*ECORS-CROP DSS Group, 1989*] is the top of a series of duplexes of European lower crust. New advances on this particular problem are expected from the analysis of the refraction and wide-angle reflection seismic data recorded in September 1999, during another experiment which was also part of the Géofrance 3-D programme. Furthermore, additional information will be provided from the comparison of the 3-D velocity model with the gravity data, which is currently under process.

Acknowledgments. We warmly thank all the people who participated in the field work of the 1996 experiment, particularly R. Guiguet, L. Jenatton, B. Lebrun, and C. Sue. The paper benefited much from stimulating discussions inside the Géofrance 3D Alpes working group. Special thanks to M. Tardy, J.-M. Lardeaux, and P. Ledru for their support and to E. Kissling and C. Papazachos for their constructive reviews. Most figures were plotted using the GMT software package. Numerical computations were performed at the Service Commun de Calcul Intensif de l'Observatoire de Grenoble. This is Géofrance-3D publication 112.

References

Berckhemer H., Topographie des Ivrea-Körpers, abgeleitet aus seismischen und gravimetrischen Daten, *Schweiz. Mineral. Petrogr. Mitt., 48,* 235-246, 1968.

Cattaneo, M., P. Augliera, S. Parolai, and D. Spallarossa, Anomalously deep earthquakes in northwestern Italy, *J. Seismol., 3,* 421-435, 1999.

Christensen, N.I., Poissons's ratio and crustal seismology, *J. Geophys. Res., 101,* 3139-3156, 1996.

Closs H., and Y. Labrouste, Recherches séismologiques dans les Alpes occidentales au moyen de grandes explosions en 1956, 1958 et 1960, *Mém. Coll. Ann. Géophys. Int., 12,* 241 pp., CNRS, Paris, 1963.

Eberhart-Phillips, D., Local earthquake tomography : earthquake source regions, in *Seismic Tomography: Theory and Practice,* edited by H.M. Iyer and K. Irahara, pp. 613-643, Chapman and Hall, New York, 1993.

ECORS-CROP Deep Seismic Sounding (DSS) Group, A new picture of the Moho under the western Alps, *Nature, 337,* 249-251, 1989.

Evans, J.R., D. Eberhart-Phillips, and C.H. Thurber, User's manual for SIMULPS12 for imaging V_P and V_P/V_S: A derivative of the "Thurber" tomographic inversion SIMUL3 for local earthquakes and explosions, *U.S. Geol. Surv. Open File Rep., 94-431,* 1994.

Froidevaux, P., and A. Guillaume, Contribution à l'analyse structurale des Alpes liguro-piémontaises par l'étude du champ magnétique terrestre, *Tectonophysics, 54,* 139-157, 1979.

Groupe de Recherche Géofrance 3D, Géofrance 3D: L'imagerie géologique et géophysique du sous-sol de la France, *Mém. Soc. Géol. Fr., 172,* 53-71, 1997.

Haslinger, F., E. Kissling, J. Ansorge, D. Hatzfeld, E. Papadimitriou, V. Karakostas, K. Makropoulos, H.-G. Kahle, and Y. Peter, 3D crustal structure from local earthquake tomography around the Gulf of Arta (Ionian region, NW Greece), *Tectonophysics, 304,* 201-218, 1999.

Hauksson, E., and J.S. Haase, Three-dimensional V_P and V_P/V_S velocity models of the Los Angeles basin and central Transverse Ranges, California, *J. Geophys. Res., 102,* 5423-5453, 1997.

Kissling, E., Deep structure of the Alps - what do we really know? *Phys. Earth Planet. Inter., 79,* 87-112, 1993.

Kissling, E., W.L. Ellsworth, and R. Cockerham, Three-dimensional structure of the Long Valley Caldera, California, region by geotomography, *U.S. Geol. Surv. Open File Rep., 84-939,* 188-220, 1984.

Kissling, E., W.L. Ellsworth, D. Eberhart-Phillips, and U. Kradolfer, Initial reference models in local earthquake tomography, *J. Geophys. Res., 99,* 19,635-19,646, 1994.

Lanza, R., Profili magnatici et di gravità nelle Alpi occidentali, *Riv. It. Geofis., 11,* 175-183, 1975.

Lee, W.H., and J.E. Lahr, HYPO71: A computer program for determining hypocenter, magnitude and first-motion pattern of local earthquakes, *U.S. Geol. Surv. Open File Rep., 75-331,* 1975.

Masson, F., J. Verdun, R. Bayer, and N. Debeglia, Une nouvelle carte gravimétrique des Alpes occidentales et ses conséquences structurales et tectoniques, *C.R. Acad. Sci., Ser. IIA, 329,* 865-871, 1999.

Ménard, G., and P. Molnar, Collapse of a Hercynian Tibetan Plateau into a late Paleozoic European Basin and Range province, *Nature, 334,* 235-237, 1988.

Ménard, G., and F. Thouvenot, Ecaillage de la lithosphère européenne sous les Alpes occidentales: arguments gravimétriques et sismiques liés à l'anomalie d'Ivrea, *Bull. Soc. Géol. Fr., XXVI,* 875-884, 1984.

Michelini, A., and T.V. Mac Evilly, Seismological studies at Parkfield, I, Simultaneous inversion for velocity structure and hypocenters using cubic B-splines parameterization, *Bull. Seismol. Soc. Am., 81,* 524-552, 1991.

Nicolas, A., A. Hirn, R. Nicolich, R. Polino, and ECORS-CROP Working Group, Lithospheric wedging in the western Alps inferred from the ECORS-CROP traverse, *Geology, 18,* 587-190, 1990.

Ritz, J-F., Evolution du champ de contraintes dans les Alpes du Sud depuis la fin de l'Oligocène- Implications sismotectoniques, Ph.D. thesis, 187 pp., Univ. Montpellier II, Montpellier, France, 1991.

Rothé, J-P., Les séismes des Alpes françaises en 1938 et la séismicité des Alpes occidentales, *Ann. Inst. Phys. Globe Strasbourg, 3,* 1-105, 1941.

Roure, F., R. Polino, and R. Nicolich, Early Neogene deformation beneath the Po Plain: Constraints on the postcollisional Alpine evolution, in *Deep Structure of the Alps,* edited by F. Roure et al., *Mém. Soc. Géol. Fr., 156,* 309-322, 1990.

Roure, F., P. Choukroune, and R. Polino, Deep seimic reflection data and new insights on the bulk geometry of mountain ranges, *C.R. Acad. Sci., Ser. IIA, 322,* 345-359, 1996.

Schmid, S.M., and E. Kissling, The arc of the western Alps in the light of geophysical data on deep crustal structure, *Tectonics, 19,* 62-85, 2000.

Schwartz, S., La zone Piémontaise des Alpes occidentales: un paléo-complexe de subduction. Arguments métamorphiques, géochronologiques et structuraux, Ph.D. thesis, 341 pp., Univ. Claude Bernard Lyon I, Lyon, France, 2000.

Schwartz, S., J.M. Lardeaux, A. Paul, P. Tricart, and G. Poupeau, Significance of syn-convergence extension in the western Alps revealed by fission track analysis and geophysical modelling (abstract), 4th workshop on Alpine Geological Studies, Tübingen, *Tübingen Geowiss. Arbeit., Ser. A, 52,* 18-19, 1999.

Schwartz, S., J.M. Lardeaux, S. Guillot, and P. Tricart, Diversité du métamorphisme éclogitique au sein du massif ophiolitique du Monviso (Alpes occidentales, Italie), *Geodin. Acta, 13,* 169-188, 2000.

Sellami, S., E. Kissling, F. Thouvenot, and J. Fréchet, Initial reference velocity model for seismic tomography in the western Alps, *Abstract Suppl. E.G.S. XX*, Eur. Geophys. Soc., Hamburg, Germany, 1995.

Solarino, S., E. Kissling, S. Sellami, S. Smriglio, F. Thouvenot, M. Granet, K.P. Bonjer and D. Sleijko, Compilation of a recent seismicity data base of the greater Alpine region from several seismological networks and preliminary 3D tomographic results, *Ann. di Geofis., XL,* 161-174, 1997.

Sue, C., Dynamique actuelle et récente des Alpes occidentales internes, Ph.D. thesis, 300 pp., Univ. Joseph Fourier, Grenoble, France, 1998.

Sue, C., and P. Tricart, Late alpine brittle extension above the Frontal Pennine thrust near Briançon, France, *Eclogae Geol. Helv., 92,* 171-181, 1999.

Sue, C., F. Thouvenot, J. Fréchet, and P. Tricart, Widespread extension in the core of the western Alps revealed by earthquake analysis, *J. Geophys. Res., 104,* 25,611-25,622, 1999.

Thouvenot, F., Aspects géophysiques et structuraux des Alpes occidentales et de trois autres orogènes (Atlas, Pyrénées, Oural), thesis, 378 pp., Univ. Joseph Fourier, Grenoble, France, 1996.

Thurber, C.H., Earthquake locations and three-dimensional crustal structure in the Coyote Lake area, central California, *J. Geophys. Res., 88,* 8226-8236, 1983.

Thurber, C.H., Local earthquake tomography: Velocities and V_P/V_S - Theory, in *Seismic Tomography: Theory and Practice,* pp. 563-583, edited by H.M. Iyer and K. Irahara, Chapman and Hall, New York, 1993.

Toomey, D.R., and G.R. Foulger, Tomographic inversion of local earthquake data from the Hengill-Grensdalur central volcano complex, Iceland, *J. Geophys. Res., 94,* 17497-17510, 1989.

Um, J., and C.H. Thurber, A fast algorithm for two-point seismic ray tracing, *Bull. Seismol. Soc. Am., 77,* 972-986, 1987.

Waldhauser, F., E. Kissling, J. Ansorge, and St. Mueller, Three-dimensional interface modelling with two-dimensional seismic data: The Alpine crust-mantle boundary, *Geophys. J. Int., 135,* 264-278, 1998.

N. Béthoux, Géosciences Azur, Université de Nice and CNRS, 250 rue Albert Einstein, 06560 Valbonne, France. (bethoux@geoazur.unice.fr)

M. Cattaneo, Istituto Nazionale di Geofisica, Via di Vigna Murata 605, 00143 Roma, Italy. (cattaneo@ingrm.it)

J. Fréchet, A. Paul, and F. Thouvenot, Laboratoire de Géophysique Interne et Tectonophysique, CNRS and Université Joseph Fourier, BP 53, 38041 Grenoble Cedex 9, France. (Julien.Frechet@ujf-grenoble.fr; Anne.Paul@ujf-grenoble.fr; Francois.Thouvenot@ujf-grenoble.fr)

D. Spallarossa, Dipartimento Scienze della Terra, Università di Genova, Viale Benedetto XV, 5, 16132 Genova, Italy. (daniele@dister.unige.it)

(Received March 23, 2000; revised March 23, 2001;
accepted April 7, 2001.)

---

[1] Laboratoire de Géophysique Interne et Tectonophysique, CNRS and Université Joseph Fourier, Grenoble, France.

[2] Dipartimento Scienze della Terra, Università di Genova, Genova, Italy.

[3] Now at Istituto Nazionale di Geofisica, Roma, Italy.

[4] Géosciences Azur, Université de Nice and CNRS, Nice, France.

Paper number 2001JB000388.
0148-0277/01/2001JB000388$09.00

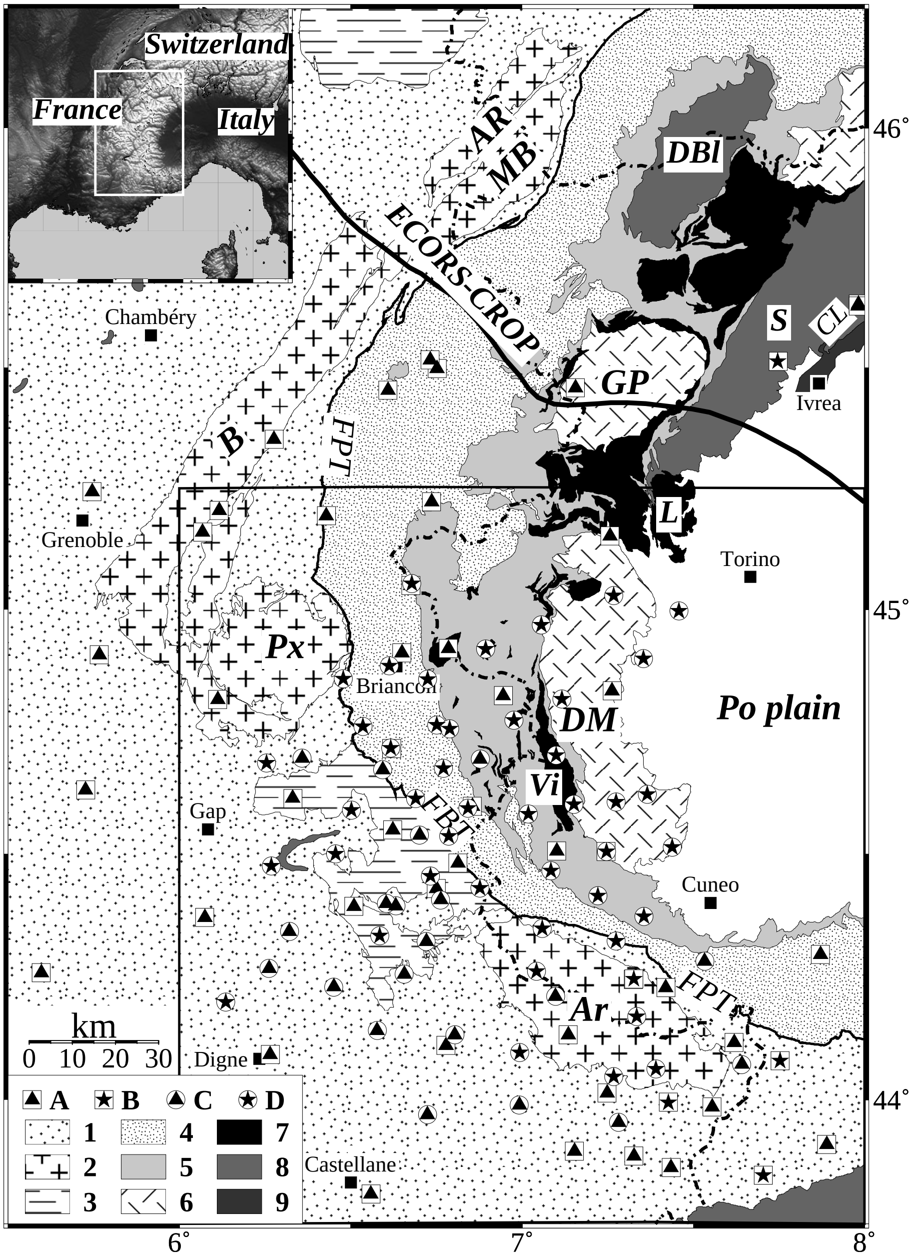

Figure 1: Simplified structural map of the western Alps. Three-component and single-component stations (permanent and temporary) are plotted as solid stars and solid triangles, respectively. Note that six stations used in this study are located slightly out of the region shown on the map. The study region represented in subsequent figures is outlined by the box. A, single-component permanent seismic station; B, three-component permanent station; C, single-component temporary station; D, three-component temporary station; 1, Meso-cenozoic sedimentary cover of the external crystalline massifs; 2, external crystalline massifs; 3, internal nappes thrust onto the external zone (in particular, the pellicular "Flysch à Helminthoïdes" nappe); 4, Briançonnais and Sub-briançonnais Zones; 5, Piemont Zone; 6, internal crystalline massifs; 7, main ophiolites; 8, Austroalpine nappes; 9, Ivrea Zone; Ar, Argentera; DM, Dora Maira; Px, Pelvoux; Vi, Monviso; FPT, Frontal Penninic Thrust; FBT, Frontal Briançonnais Thrust; B, Belledonne; AR, Aiguilles Rouges; MB, Mont-Blanc; GP, Gran Paradiso; DBl, Dent Blanche; S, Sesia Zone; L, Lanzo massif; CL, Canavese Line.

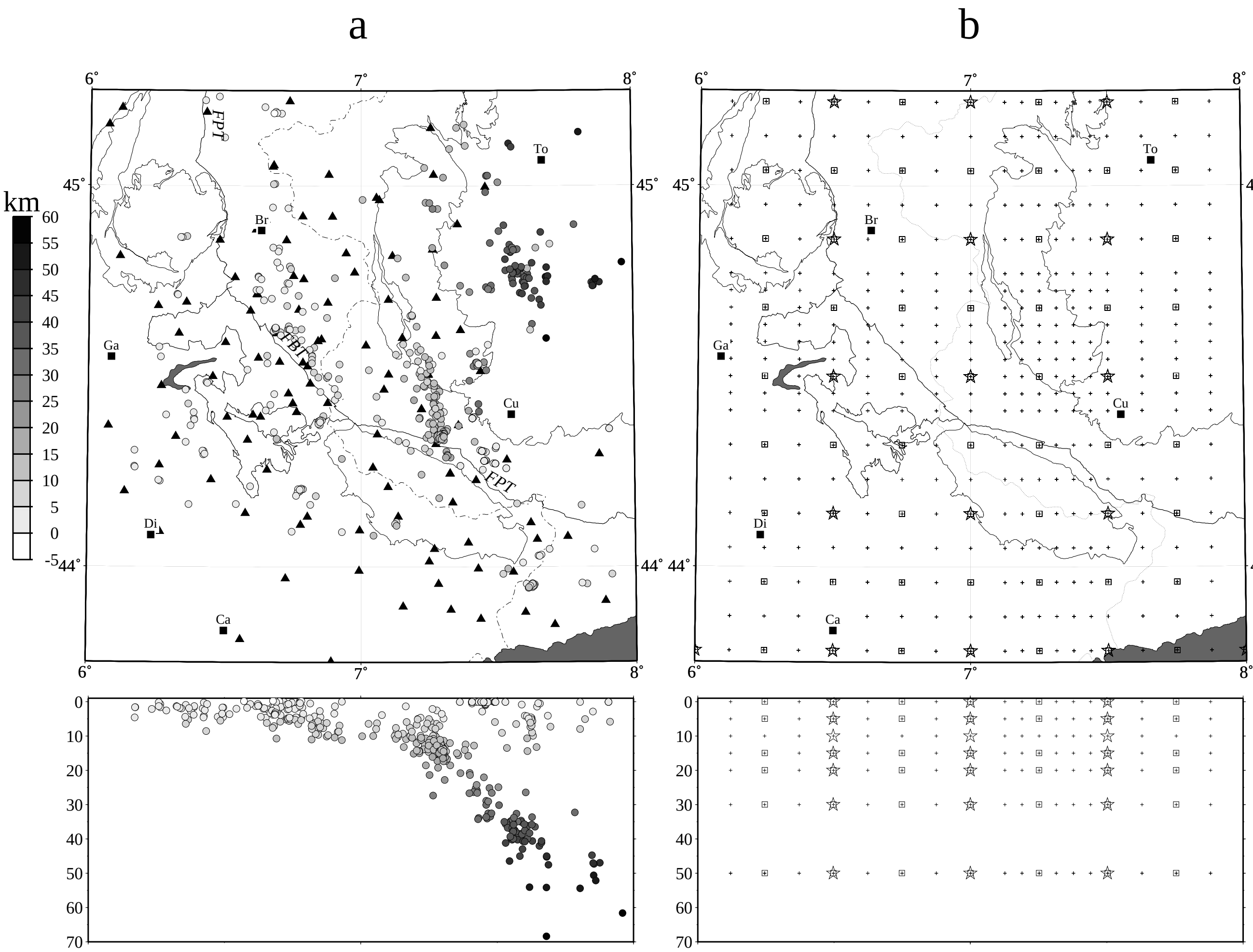

Figure 2: (a) Locations of earthquakes before 3-D inversion (top) on a simplified structural map and (bottom) on an east-west cross section at a one-by-one scale. Hypocenters are plotted as shaded circles with darkness increasing with depth. Towns are Br, Briançon; Ga, Gap; To, Torino; Di, Digne; Ca, Castellane; Cu, Cuneo. (b) The three grids used in the 3-D inversion, 40 km (stars), 20 km (squares), and final short-spacing grid (5 and 10 km, crosses).

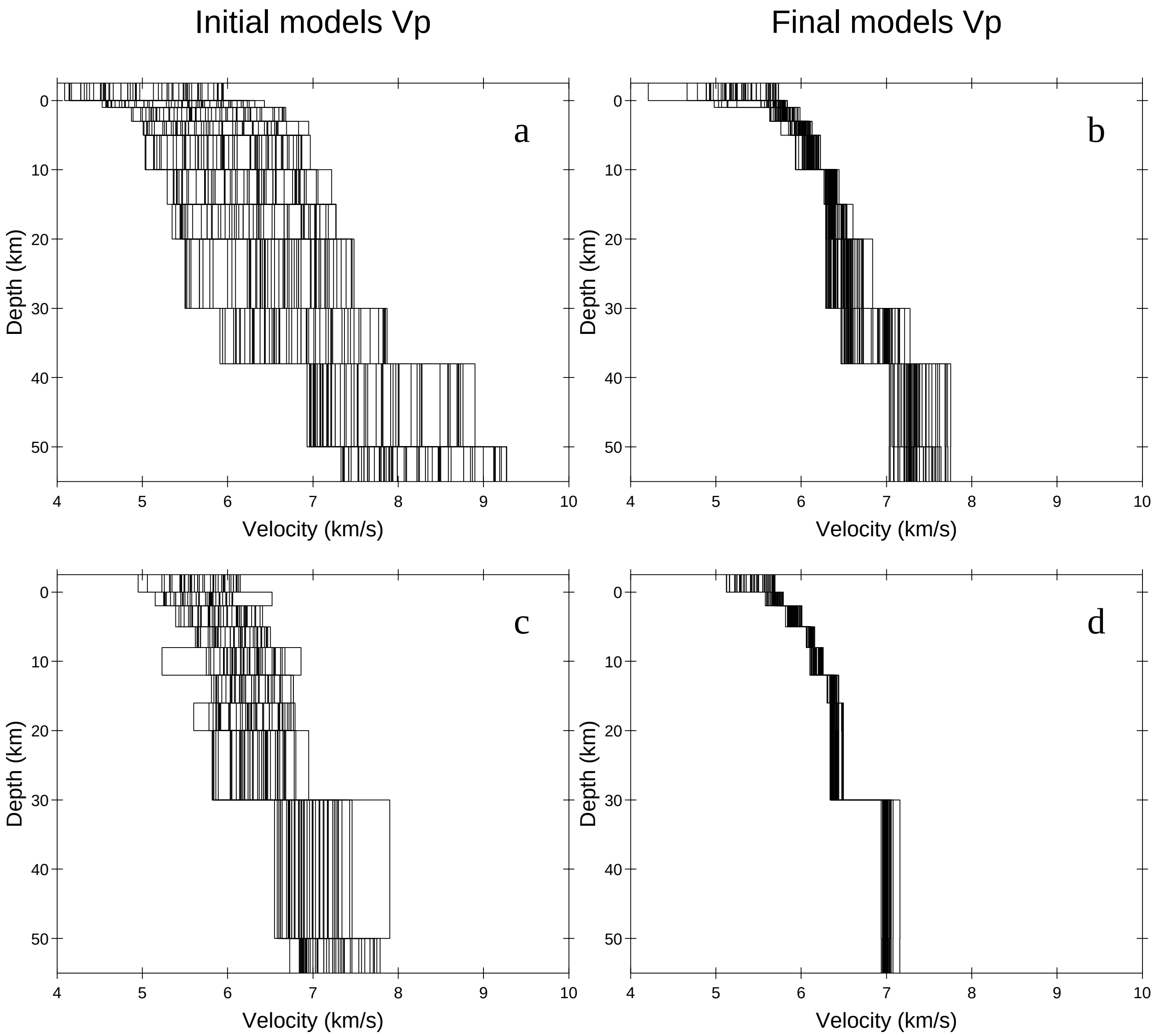

Figure 3: Results of the inversion for a 1-D model (V_P). Note that we do not show velocites in the half-space (z > 60 km) because they are not reliable. (a) One hundred random initial V_P models generated from the updated a priori model. (b) The 61 resulting models giving a variance smaller than 0.15 s^2 after 10 iterations. Note the convergence to a narrow distribution of V_P between 2 and 20 km depth. (c) The 50 new random initial models generated from the best model of Figure 3b modified to suppress too thin layers in poorly resolved depth zones. (d) Final result of 1-D inversion: 46 models are plotted. Note the concentration of velocities around a single model which was consequently chosen as initial reference model in the 3-D inversion.

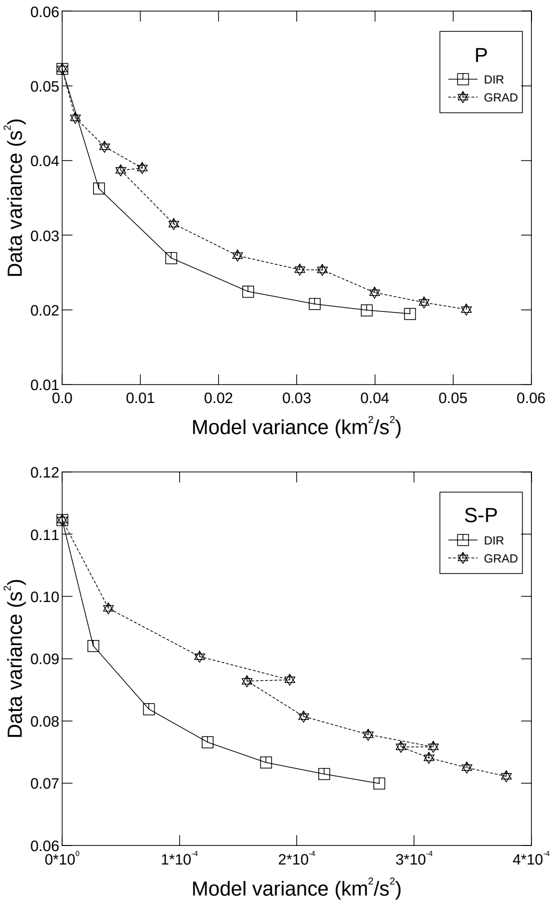

Figure 4: Data misfit versus model length for (top) P and (bottom) S-P data sets for the direct (DIR) and gradational (GRAD) inversions.

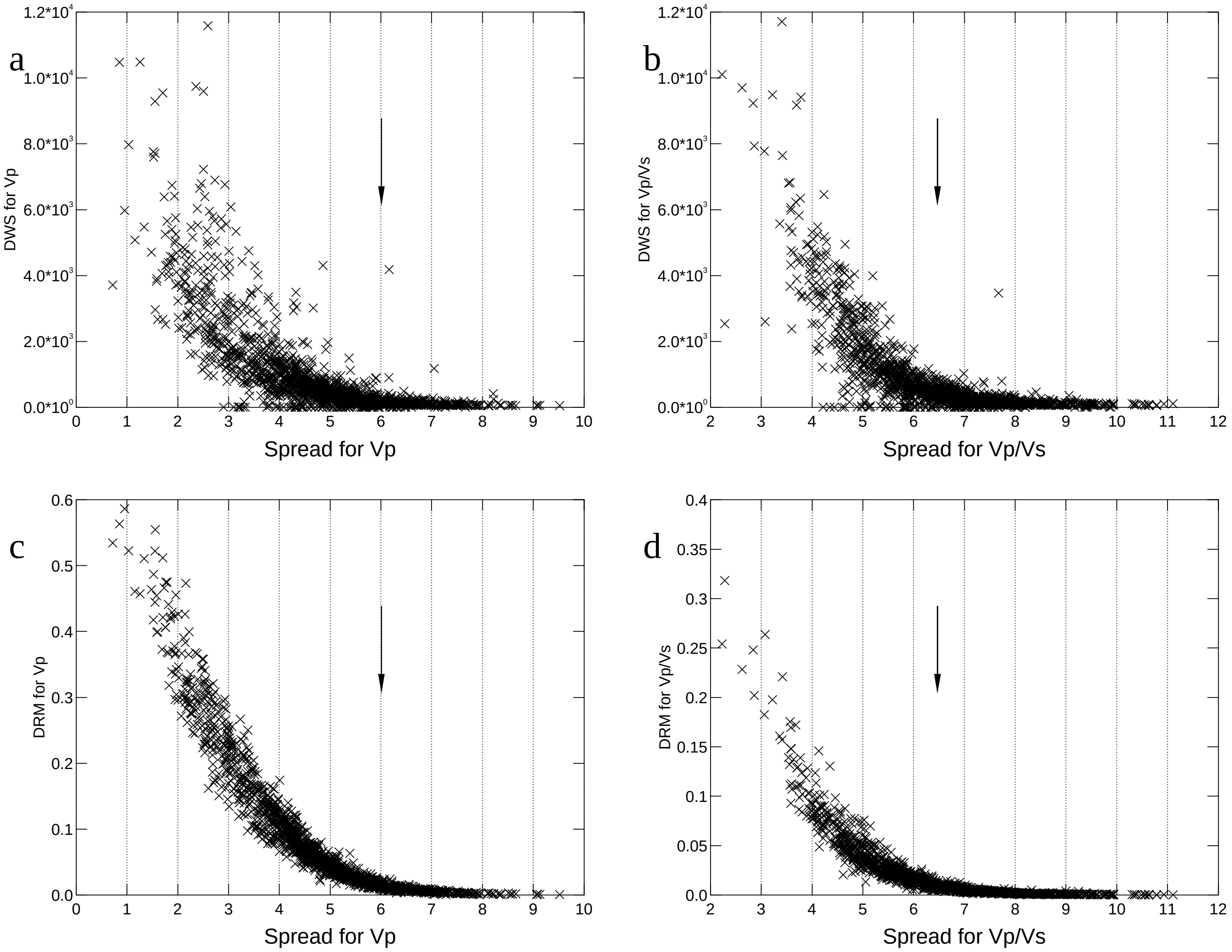

Figure 5: (a, b) Derivative weight sum (DWS) and (c, d) diagonal value of the resolution matrix (DRM) versus spread function values for V_P (Figures 5a and 5c) and V_P/V_S (Figures 5b and 5d) models computed from the direct inversion for the fine grid. The arrows indicate the threshold of spread-function chosen to delineate poorly resolved areas in subsequent velocity maps.

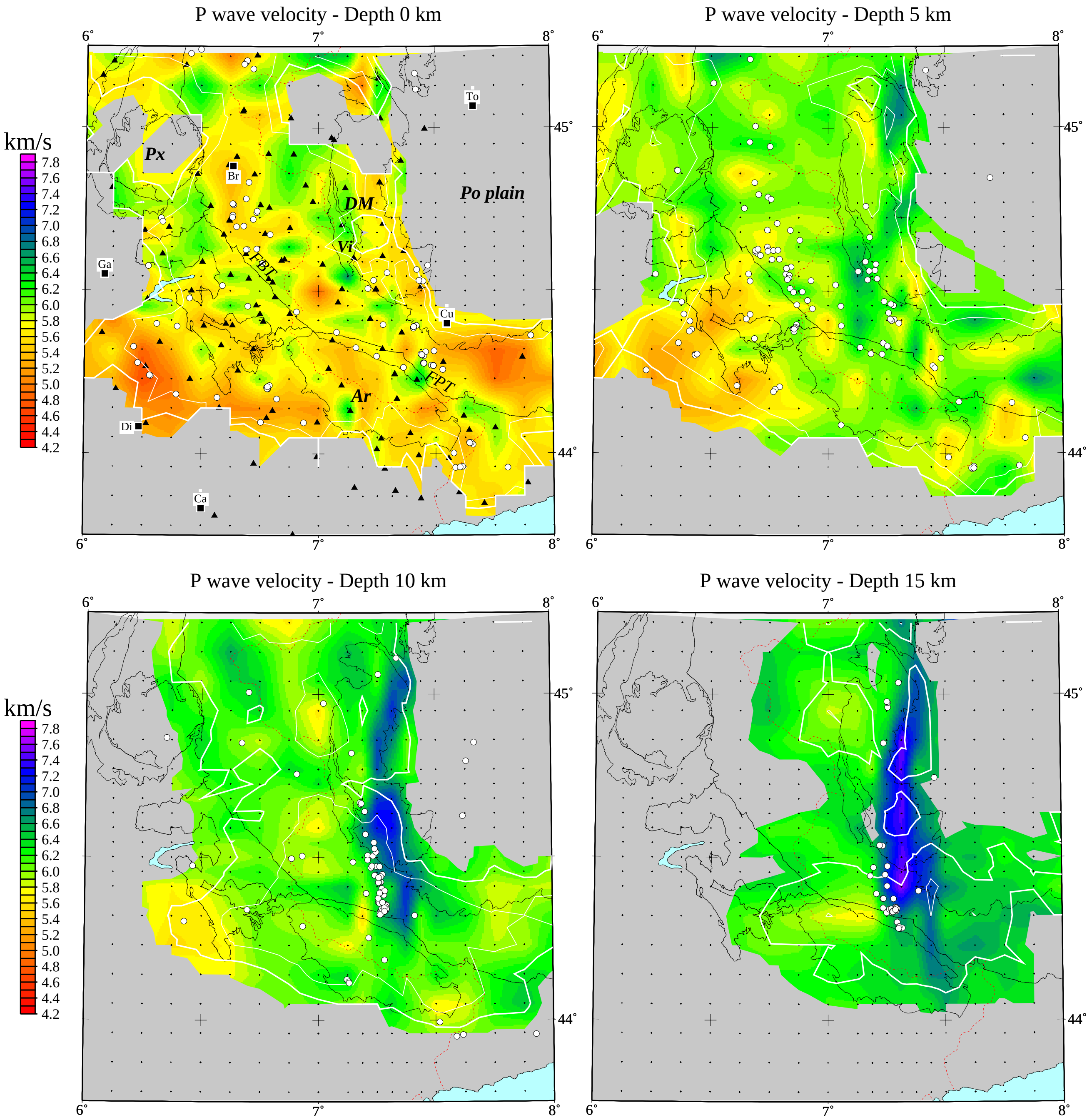

Plate 1a: Map view slices of the 3-D V_P model computed from direct inversion. (a) Slices at 0, 5, 10, and 15 km depth. Unresolved regions with spread function values larger than 6 are shaded. The thick and thin white lines are the 5 and 4 contours of the spread function of the resolution matrix. Hypocenters located in a 5-km-thick depth slice centered on the layer depth are plotted as white circles on each map. In the map view at 30 km, the depth range considered for hypocenters is 10 km. Station locations are plotted as black triangles on the 0-km depth slice. Each map shows the velocity grid nodes as black dots. The main structural contours simplified from Figure 1 are plotted as black lines. The dotted red line is the border between France and Italy. Abbreviations are the same as in Figures 1 and 2.

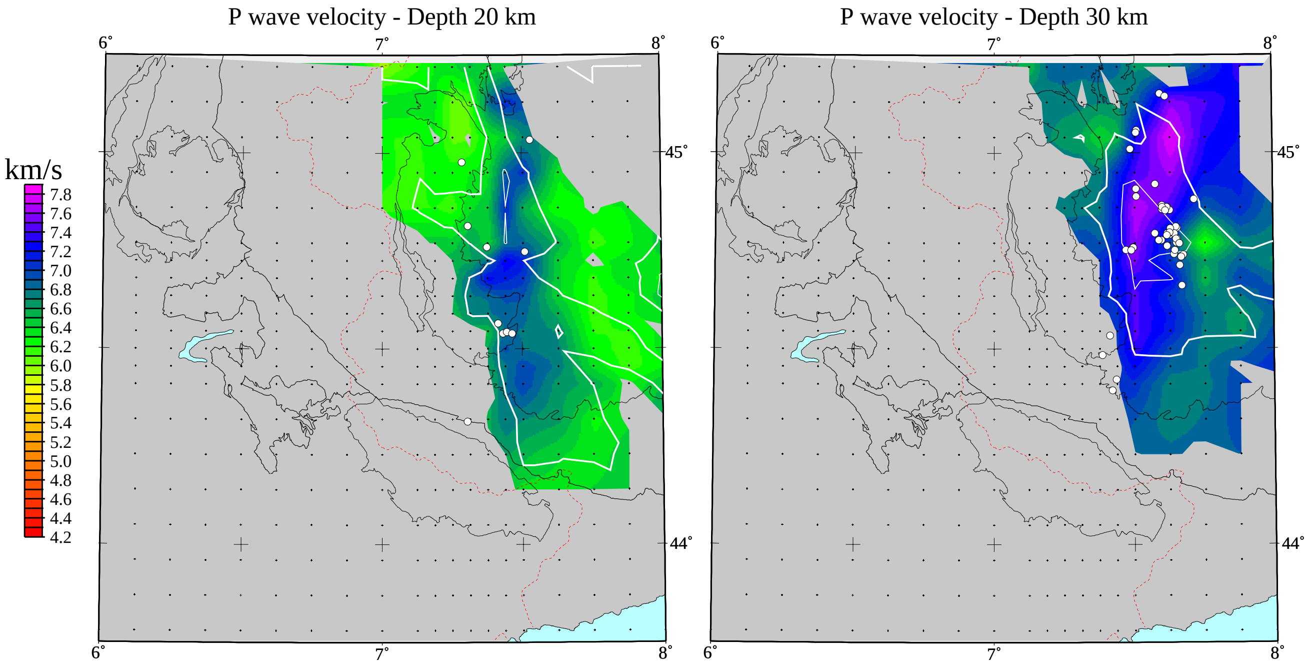

P wave velocity - Depth 20 km

P wave velocity - Depth 30 km

Plate 1b: Same as Plate 1a except for slices at 20 and 30 km depth.

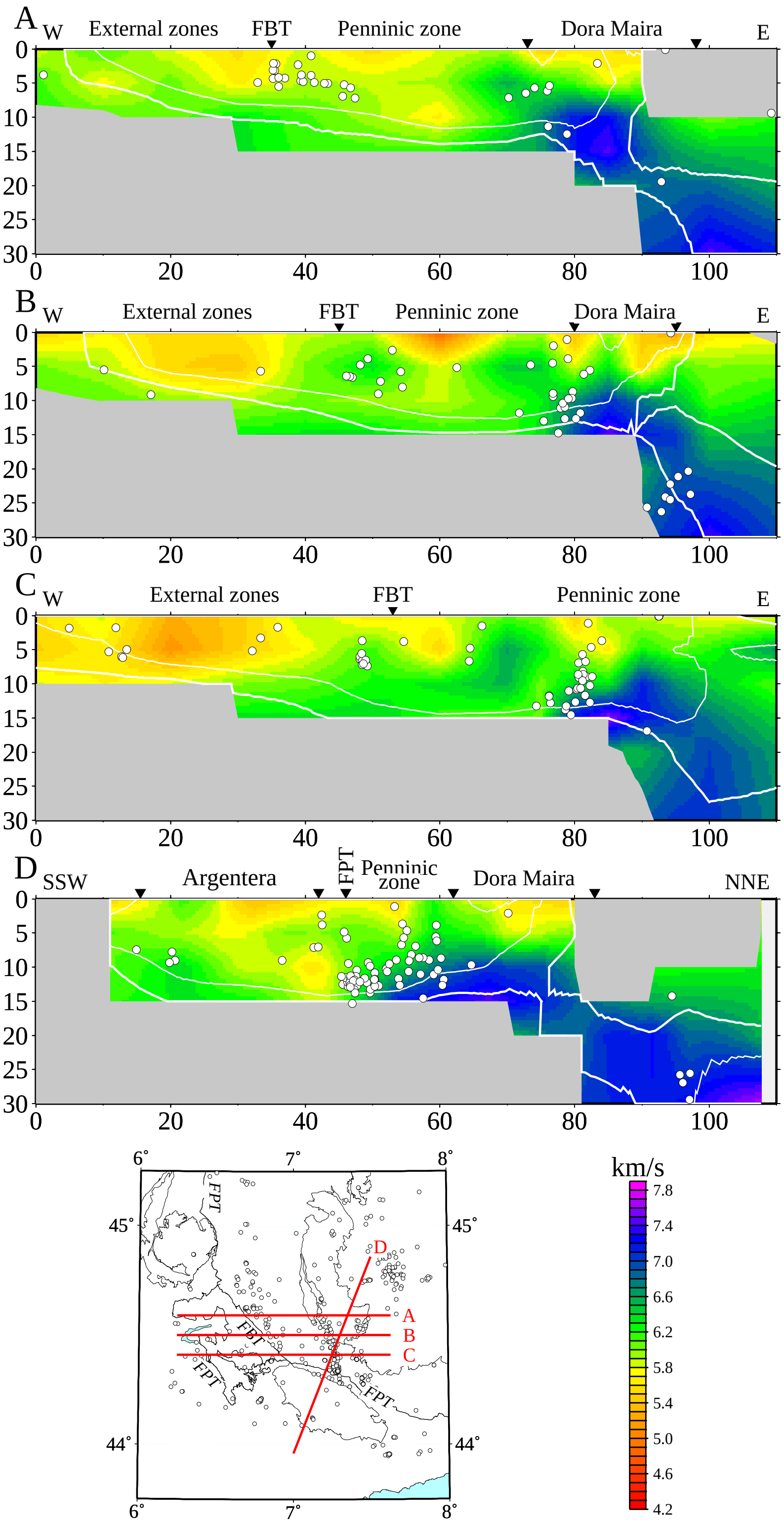

Plate 2: Depth cross sections through the V_P model along lines A, B, C, and D, the locations of which are plotted on the map at bottom. As in Plate 1, unresolved zones with spread function values larger than 6 are shaded. The thick and thin white lines show the 5 and 4 contours of the spread function. White circles are hypocenters located $\leq$ 5 km from the profiles.

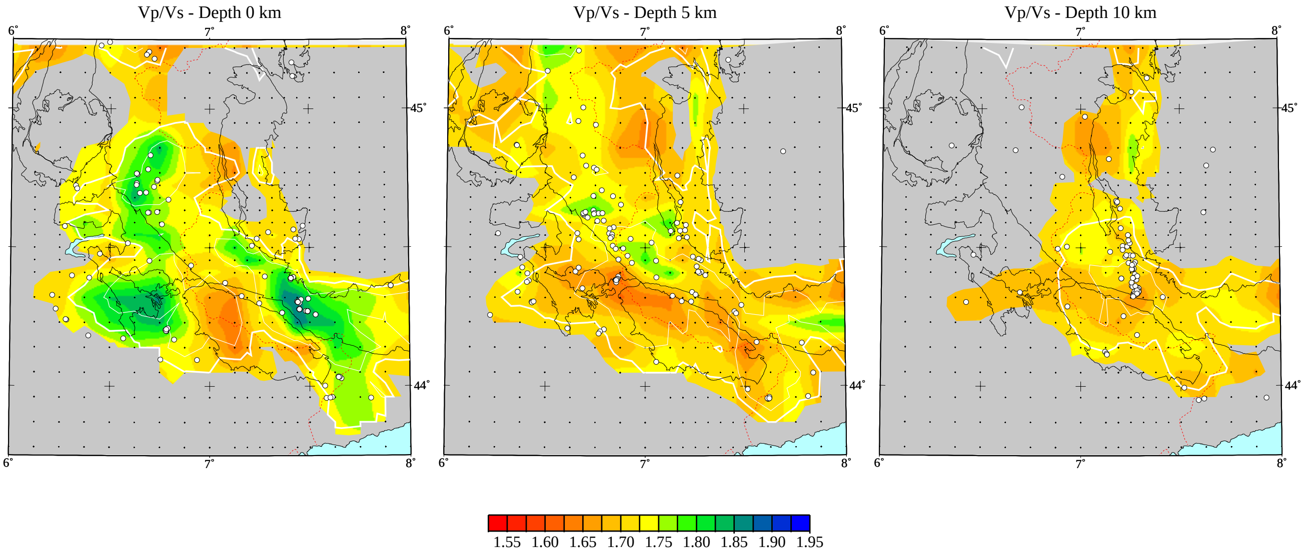

Plate 3: Map view slices of the V_P/V_S model at 0, 5, and 10 km depth. Unresolved regions (spread function values larger than 6.5) are shaded. The 4.5 and 5.5 contours of the spread function are plotted as a thin and a thick white line. The white circles are hypocenters located in the 5-km-thick depth range of the slice. The nodes of the grid used in the inversion are shown as black dots.

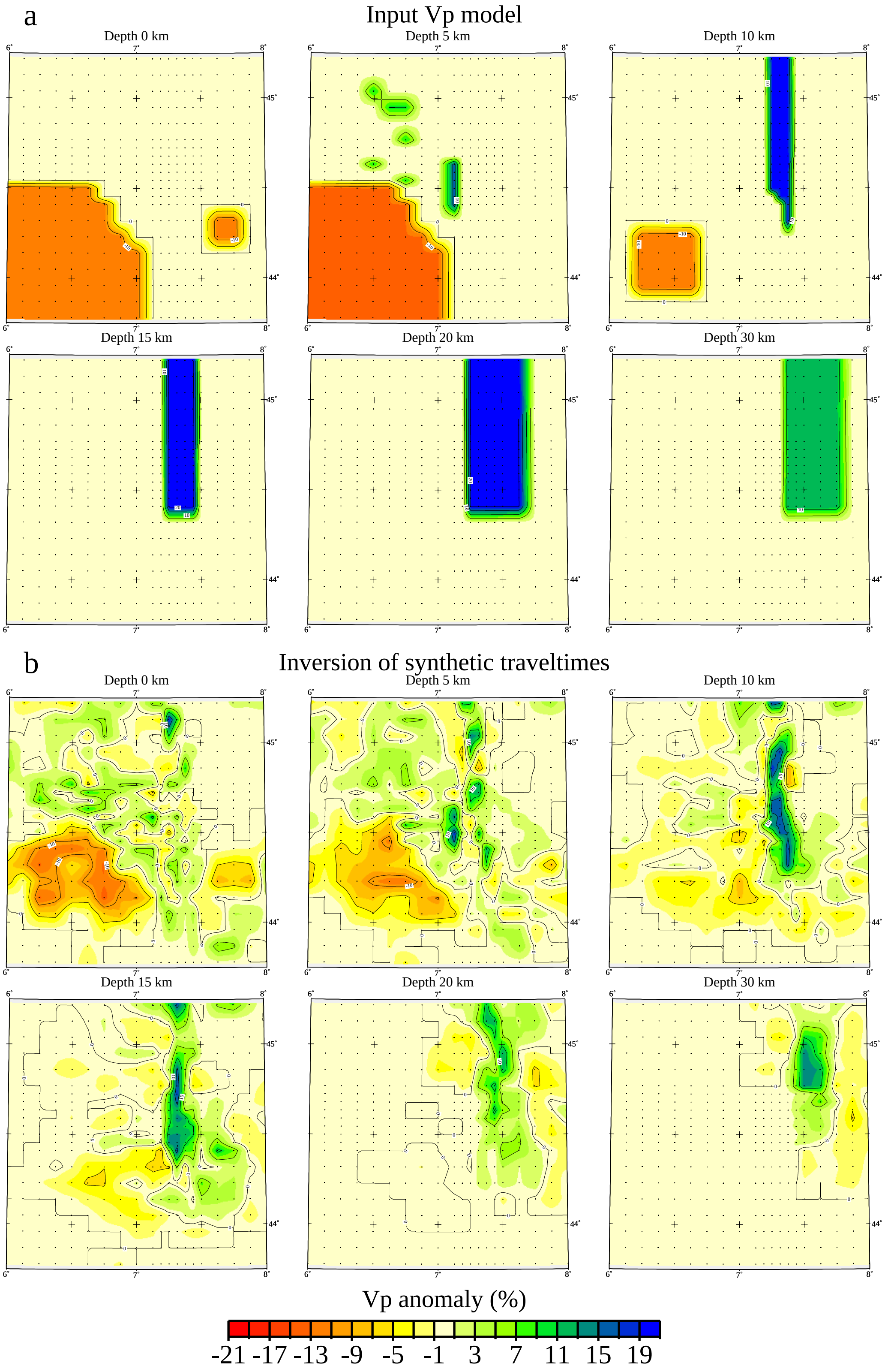

Plate 4: (a) Depth slices of the input synthetic *P* velocity model set up to test the resolution of the inversion. (b) Results of the inversion of the set of travel times computed in the model shown in Plate 4a.

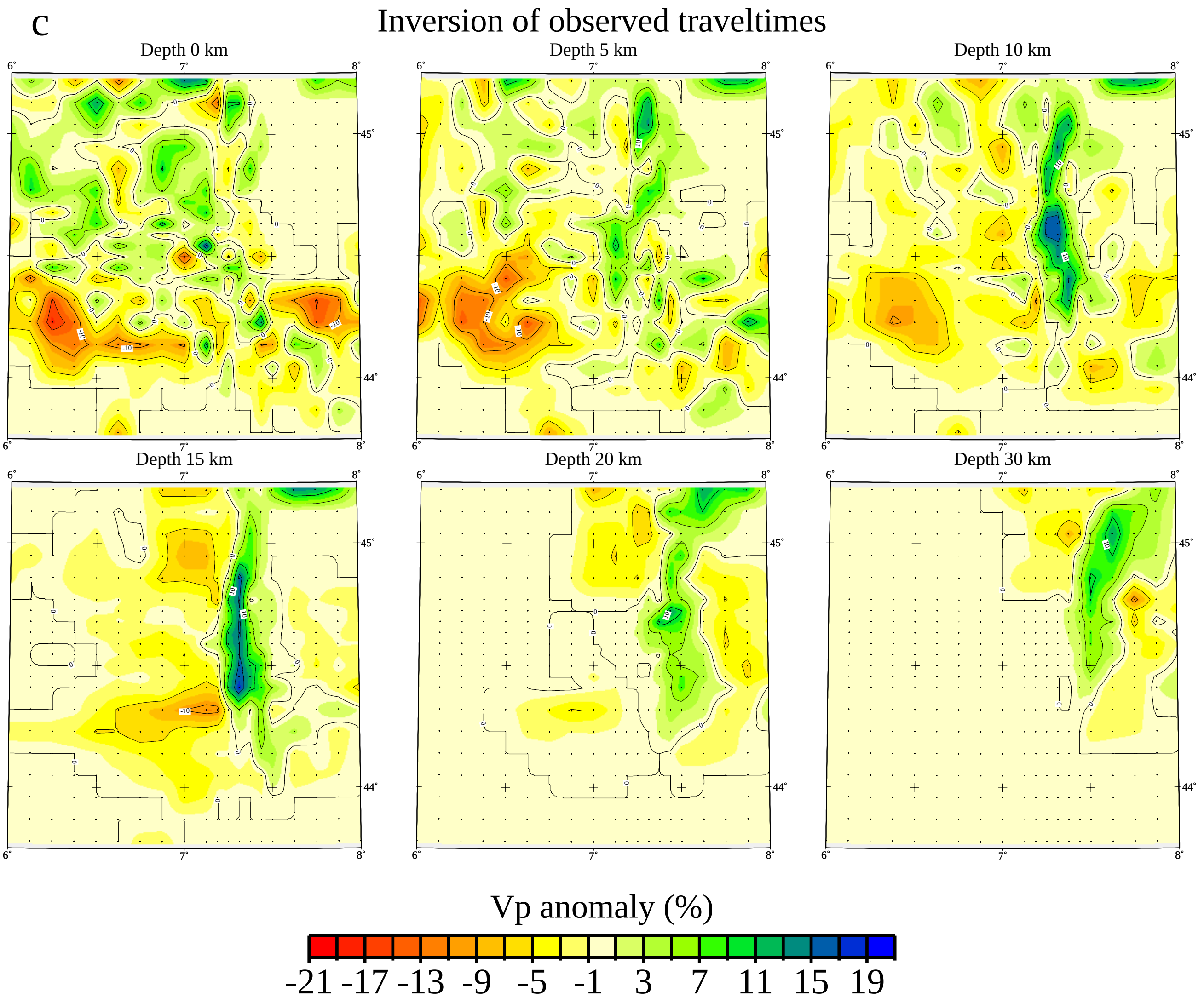

Plate 4c: Results of the inversion of observed travel times (same as Plate 1) plotted using the same color scale as Plate 4b for comparison. Note that here we plot the variations (in percents) of V_P with respect to the initial 1-D model.

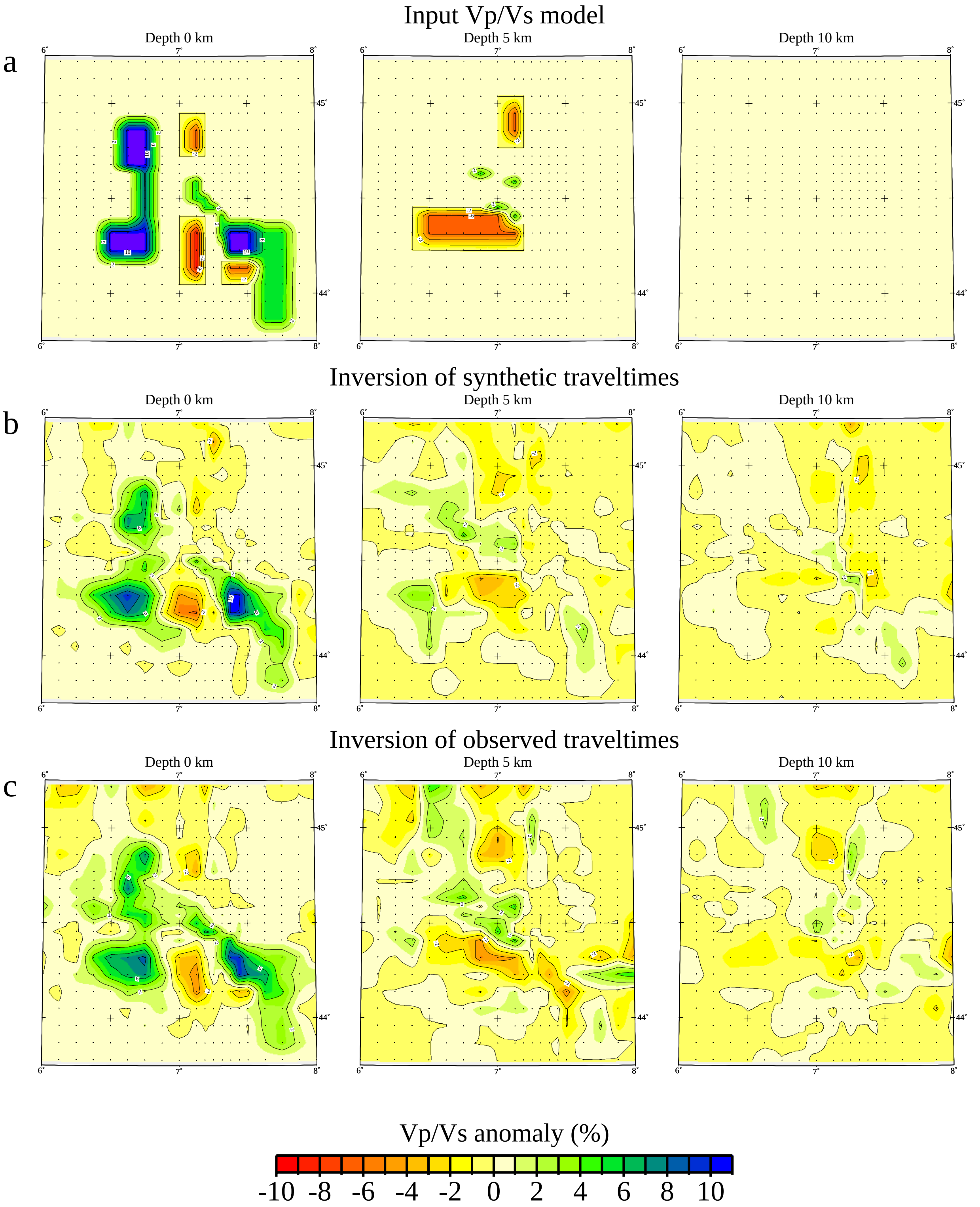

Plate 5: (a) The 0-, 5- and 10-km-depth slices of the synthetic V_P/V_S model set up to test the resolution of the inversion. (b) Results of the inversion of the set of travel times computed in the model shown in Plate 5a. (c) Results of the inversion of observed travel times (same as Plate 3). As in Plate 4, the color scale shows variations in V_P/V_S with respect to the homogeneous (V_P/V_S=1.71) initial model.

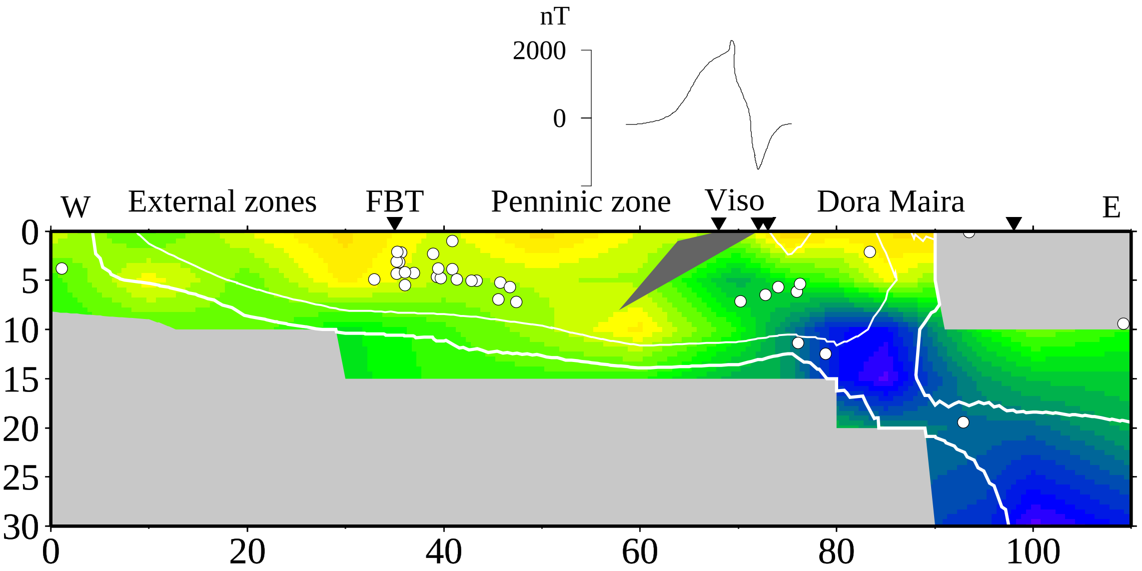

Plate 6: Comparison between the velocity structure along cross section A of Plate 2 and the high-susceptibility body (shaded) modeled by *Lanza* [1975] to explain the strong anomaly of the total intensity of the magnetic field measured along the same line and plotted at the top.

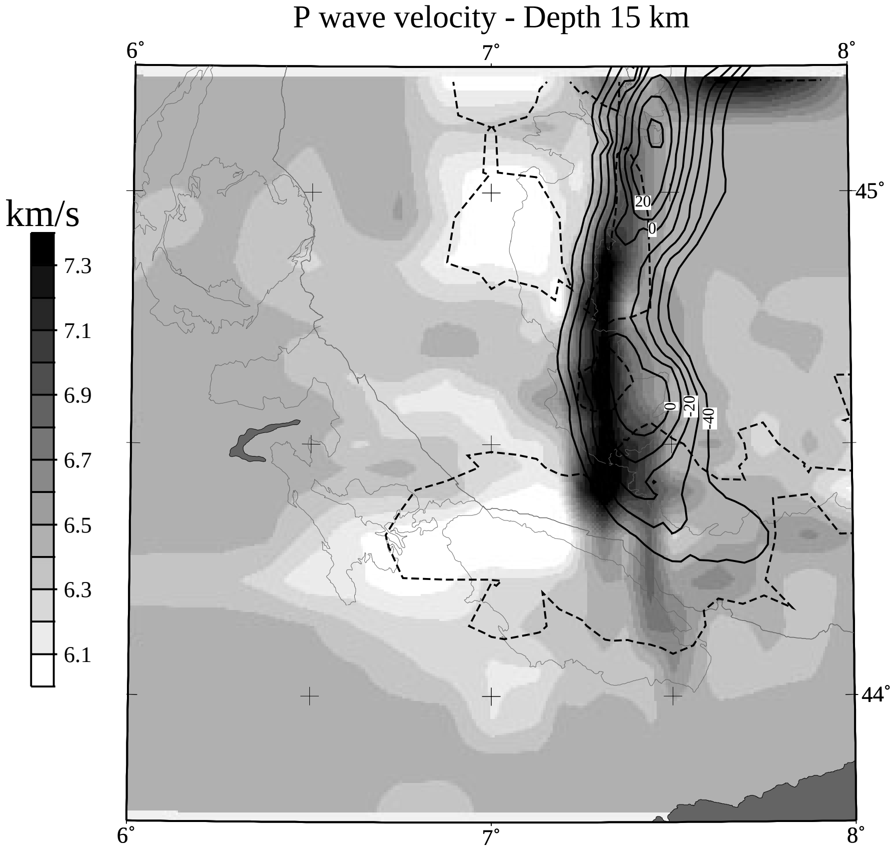

Figure 6: Comparison between the high velocity anomaly at 15-km depth and the strong positive Bouguer anomaly associated with the Ivrea body. Only isolines for anomaly values larger than -40 mGal are plotted with a spacing of 10 mGal. The dotted line is the 5 contour of the spread function of the resolution matrix. Gravity data were compiled by *Masson et al.* [1999].